



**1 Comprehensive evaluation of typical planetary boundary
2 layer (PBL) parameterization schemes in China. Part I:
3 Understanding expressiveness of schemes for different
4 regions from the mechanism perspective**

5 Wenxing Jia¹, Xiaoye Zhang^{1,2*}, Hong Wang¹, Yaqiang Wang¹, Deying Wang¹, Junting Zhong¹,
6 Wenjie Zhang¹, Lei Zhang¹, Lifeng Guo¹, Yadong Lei¹, Jizhi Wang¹, Yuanqin Yang¹, Yi Lin³

7 ¹State Key Laboratory of Severe Weather & Key Laboratory of Atmospheric Chemistry of CMA,
8 Chinese Academy of Meteorological Sciences, Beijing, 100081, China

9 ²Center for Excellence in Regional Atmospheric Environment, IUE, Chinese Academy of Sciences,
10 Xiamen, 361021, China

11 ³Key Laboratory for Mesoscale Severe Weather, Ministry of Education, and School of Atmospheric
12 Sciences, Nanjing University, Nanjing, China

13 Correspondence to: X. Zhang (xiaoye@cma.gov.cn)

14
15
16
17
18
19
20
21
22
23
24
25
26
27
28
29
30
31
32
33



34 **Abstract.** The optimal choice of the planetary boundary layer (PBL) parameterization scheme is of
35 particular interest and urgency to a wide range of scholars, especially for many works involving
36 models. At present, there have been many works to evaluate the PBL schemes. However, little
37 research has been conducted into a more comprehensive and systematic assessment of the
38 performance capability of schemes in key regions of China, especially when it comes to the
39 differences in the mechanisms of the schemes themselves, primarily because there's scarcely
40 sufficient observational data, computer resources, and storage support to complete the work. In
41 addition, there are many factors that influence the selection of schemes, such as underlying surface,
42 initial and boundary conditions, near-surface layer scheme, horizontal/vertical resolution, etc. In
43 this Part (i.e., Part I), four typical schemes (i.e., YSU, ACM2, BL and MYJ) are selected to
44 systematically analyze and evaluate near-surface meteorological parameters, PBL vertical structure,
45 PBL height (PBLH), and turbulent diffusion in five key regions (i.e., North China Plain, NCP;
46 Yangtze River Delta, YRD; Sichuan Basin, SB; Pearl River Delta, PRD and North west Semi-arid,
47 NS) of China in different seasons (i.e., January, April, July and October). The differences in the
48 simulated 2-m temperatures between the nonlocal closure schemes are mainly affected by the
49 downward shortwave radiation, but to compare the nonlocal closure schemes with the local closure
50 schemes, the effect of sensible heat flux needs to be further considered. In terms of temporal
51 variation, the simulated results for July are better than the other three months, and the simulated
52 results for nighttime are better than daytime. In terms of regional distribution, the temperature at
53 stations with higher elevation is easily underestimated, while overestimated with lower elevation.
54 The variation of relative humidity corresponds to temperature. The 10-m wind speed is under the
55 influence of factors like the momentum transfer coefficient and the integrated similarity functions
56 at night. The wind speeds are more significantly overestimated in the plains and basin, while less
57 overestimated or even underestimated in the mountains, as a result of the effect on topographic
58 smoothing in the model. Moreover, the overestimation of small wind speeds at night is attributable
59 to the inapplicability of the Monin-Obukhov similarity theory (MOST) at night. The model captures
60 the vertical structure of temperature well, while the wind speed is outstandingly overestimated
61 below 1000 m, largely because of the turbulent diffusion coefficient (TDC). The difference between
62 the MOST and the mixing length theory, PBLH and Prandtl number is cited as the reason for the
63 difference between the TDC of the YSU and ACM2 schemes. The TDCs of the BL and MYJ
64 schemes are affected by the mixing length scale, which of BL is calculated on the basis of the effect
65 of buoyancy, while MYJ calculates it with the consideration of the effect of the total turbulent
66 kinetic energy. The PBLH of the BL scheme is better than the other schemes because of the better
67 simulation results of temperature. The difference in the PBLH by the YSU and ACM2 scheme
68 mainly comes from the Richardson number and the jagged PBLH of the MYJ scheme is due to the
69 coarse vertical resolution and the threshold value.



70 In general, to select the optimal scheme, it is necessary to offer different options for different regions
71 with different focuses (heat or momentum). (1) Temperature field. The BL scheme is recommended
72 for January in the NCP region, especially for Beijing, and the MYJ scheme is better for the other
73 three months. The ACM2 scheme would be a good match for the YRD region, where the simulation
74 differences between the four schemes are small. The topography of the SB region is more complex,
75 but for most of the areas in the basin, the MYJ scheme is proposed, but if more stations outside the
76 basin are involved, the BL scheme is recommended. The MYJ scheme is applied to the PRD region
77 in January and April, and the BL scheme in July and October. The MYJ scheme is counselled for
78 the NS region. (2) Wind field. The YSU scheme is recommended if the main concern is the near-
79 surface layer, and the BL scheme is suggested if focusing on the variation in the vertical direction.
80 The Part II will analyse and evaluate the factors that may influence the choice of the schemes and
81 the results of model. The final evaluation of the parameterization scheme and uncertainties will lay
82 the foundation for the improvement of the modules and forecasting of the GRAPES_CUACE
83 regional model developed independently in China.

84 1 Introduction

85 The planetary boundary layer (PBL) is the part of the troposphere that is directly influenced by the
86 force of the earth's surface with an hour or less timescale (R. B. Stull, 1988). Parameterization is the
87 determining factor in the predictive accuracy and skill as it determines key aspects of simulated
88 weather (Bauer et al., 2015; Williams, 2005). In numerical weather prediction, meagre
89 computational resources limit the resolution of the model. Following this reason, physical processes
90 cannot be resolved by the model in that the spatial scales are smaller than the model grid distance.
91 The physical module in the model that characterizes small scales relative to the model resolution is
92 called the sub-grid physical process parameterization scheme (Zhou et al., 2017). As a typical sub-
93 grid parameterization scheme, the spatial scale of turbulence is limited by the PBL height (PBLH)
94 and cannot be resolved by mesoscale weather prediction models and macroscale global climate
95 models with horizontal grid distances of magnitude of ~10 km and ~100 km. Therefore, the physical
96 module in the model that describes the effect of sub-grid turbulence on resolvable atmospheric
97 motion is called the PBL parameterization scheme. Even in the high resolution large-eddy
98 simulation (LES), small-scale turbulence requires parametric closure to characterize the role of sub-
99 grid turbulence (Deardorff, 1980). The PBL parameterization scheme controls the evolution of
100 momentum, heat, water vapor, and mass within the PBL, and the evolution of these parameters is
101 particularly affected by the turbulent diffusion coefficients (TDCs) (W. Jia and Zhang, 2021;
102 Nielsen-Gammon et al., 2010; Oke et al., 2017). Depending on the turbulence closure method, the
103 PBL parameterization schemes can be divided into three main categories: nonlocal closure schemes,



104 local closure schemes, and hybrid nonlocal-local closure schemes, and the above schemes have their
105 own advantages and disadvantages(Cohen et al., 2015; Hu et al., 2010; Wenxing Jia and Zhang,
106 2020; Xie et al., 2012).
107 Since the early 1980s, the vertical diffusion scheme based on local gradients of wind and potential
108 temperature (i.e., local K-theory) has been applied in the National Centers for Environmental
109 Prediction (NCEP). However, as pointed out by many scholars, this scheme has many deficiencies,
110 of which the most critical is that the mass and momentum transport within the PBL is mainly
111 accomplished by the large-scale eddies besides the local small-scale eddies(Roland B. Stull, 1984;
112 Wyngaard and Brost, 1984). Therefore, the new scheme developed later incorporates a counter-
113 gradient flux term to characterize the turbulent transport processes in large-scale eddies, such as
114 Medium-Range Forecast (MRF) scheme (i.e., nonlocal closure) (Hong and Pan, 1996; Troen and
115 Mahrt, 1986). This scheme has also been commonly used in China's self-developed
116 Global/Regional Assimilation and PrEdiction System (GRAPES) model because of its
117 computational simplicity and its ability to produce plausible results under typical atmospheric
118 conditions (Ma et al., 2021). Nevertheless, the MRF scheme has gradually shown some
119 shortcomings, the most typical being that when the wind speed is strong, the resulting mixing is too
120 strong and thus the PBLH is too high to be realistic(Mass et al., 2002; Persson et al., 2001). To
121 overcome this critical problem, one of the most commonly used and popular PBL parameterization
122 scheme has been introduced, which is the Yonsei University (YSU) scheme(Hong et al., 2006). YSU
123 scheme adds an additional entrainment term to the MRF scheme for explicitly calculating the
124 entrainment process of heat and momentum fluxes(Noh et al., 2003). It is still unclear why this
125 scheme is popular among scholars, either because it gives the best simulation results or simply
126 because the code of this scheme is 1, which is more convenient for the model setting. To be contrast,
127 a newer scheme, as a nonlocal scheme of the same series, has been developed that further considers
128 the issue of gray-zone of sub-grid scale turbulence, but this scheme has been rarely used and
129 evaluated (Hong and Shin, 2013).
130 Repairing the defects of local K-theory is possible by developing nonlocal closure schemes on the
131 one hand, and higher-order local closure method on the other hand. The most representative is the
132 higher-order closure scheme of the M-Y series proposed by Mellor and Yamada, such as Mellor-
133 Yamada-Janjic (MYJ) scheme and Mellor-Yamada Nakanishi and Niino Level 2.5/3
134 (MYNN2/MYNN3) scheme(Janjic, 1990, 1994; Mellor and Yamada, 1974, 1982; Nakanishi and
135 Niino, 2004). The higher-order closure schemes are capable of representing a well mixing PBL
136 structure, however, these schemes are computationally more expensive due to the addition of a
137 prognostic turbulent kinetic energy (TKE). In addition to the widely used local closure schemes of
138 the M-Y series, there is another local closure scheme that has been evaluated extensively. This
139 scheme is the Bougeault and Lacarrere (BL) scheme(Bougeault and Lacarrere, 1989), but there are



140 several differences between the BL and M-Y schemes. (1) In the parameterization of the turbulent
141 heat flux, an additional counter-gradient flux term is taken into account in the convective PBL, but
142 this counter-gradient term is different from that in the nonlocal closure scheme, which is a constant
143 ($= 0.7 \cdot 10^{-5} K cm^{-1}$) in the BL scheme. (2) The turbulent diffusion coefficient in the BL scheme
144 is calculated similarly to the M-Y schemes, but the stability functions and mixing length are different
145 from M-Y schemes.

146 In addition to the typical nonlocal closure schemes and local closure schemes, there are also hybrid
147 nonlocal-local closure schemes, typically represented by the Asymmetric Convective Model version
148 2 (ACM2) scheme. ACM2 scheme operates based on the development of ACM1 that is modified
149 based upon the Blackadar convective model(Blackadar, 1962). The upward transport within the PBL
150 is mainly by buoyancy, which is transmitted upward from the lowest level to other levels, while
151 downward is transported level-by-level(Pleim, 2007). The deficiency of the ACM1 scheme is that
152 upward transport is not better represented when the vertical resolution of the model increases. In
153 response to compensating for the shortcomings of the ACM1 scheme, the ACM2 scheme adds level-
154 by-level transport to the upward level. The ACM2 scheme have the highest universality and was
155 most suitable for the study of meteorological elements in desert region(Meng Lu et al., 2018; Wang
156 et al., 2017).

157 At present, a total of 12 PBL parameterization schemes have been developed and evaluated in the
158 currently popular mesoscale Weather Research and Forecasting (WRF) model. The continuous
159 improvement of numerical simulation techniques brings opportunities for the update and
160 development of PBL parameterization schemes. Many scholars hope that by comparing the PBL
161 parameterization schemes, they can select one scheme that better reflects the changes in
162 meteorological parameters (e.g., temperature, relative humidity and wind speed/direction),
163 pollutants and the structures of the PBL. Recent review studies have shown that although many
164 studies on the evaluation and comparison of PBL parameterization schemes have been undertaken,
165 there is still no uniform conclusion on which PBL parameterization scheme performs best(Wenxing
166 Jia and Zhang, 2020). Moreover, most of the evaluation work on PBL parameterization schemes is
167 done for individual cases or a particular region(Avolio et al., 2017; Diaz et al., 2021; Falasca et al.,
168 2021; Ferrero et al., 2018; He et al., 2022; Shen et al., 2022). In spite of those, simulation results for
169 the PBL parameterization schemes are more uniform: (1) the simulation of temperature is better
170 than that of relative humidity, and the simulation of wind speed and direction is worse. (2) The
171 simulation results of the nonlocal closure scheme are better under unstable conditions, while the
172 local closure scheme for stable conditions. However, these general conclusions are open to
173 speculation and debate(Wenxing Jia and Zhang, 2020). Many previous studies have been biased
174 towards the assessment of basic meteorological parameters, of course, which is the basic work. Due
175 to the indirect output of TDC by the model, there are fewer relevant studies to investigate the impacts



176 of turbulent diffusion on meteorological parameters. Moreover, turbulent diffusion is the key factor
177 to control the vertical mixing of momentum and scalars within the PBL. Even if there is not enough
178 turbulence observation data, it can be further analyzed and discussed according to the simulation
179 results. Aimed at remedying the current research deficiencies, this study first selects four typical
180 boundary layer parameterization schemes (nonlocal scheme: YSU, local scheme: MYJ and BL,
181 hybrid nonlocal-local scheme: ACM2) for five typical regions (NCP, YRD, SB, PRD and NS) in
182 China, and then assesses the performance capability of different PBL parameterization schemes in
183 different regions. The reasons for the differences in performance of meteorological parameters
184 between observation and simulation are illustrated in terms of temporal and regional variability.
185 Then, the mechanistic implications behind the differences are explored between schemes. In
186 addition, we further carry out the comparative analysis of the vertical structure of the PBL, turbulent
187 diffusion and the PBLH. The first part of this study (i.e., Part I) aims to be able to have a qualitative
188 and quantitative assessment of the PBL parameterization schemes in different regions for other
189 researchers to use as a reference when doing simulation studies. The second part (i.e., Part II)
190 focuses on the analysis of some uncertain factors that may affect the model simulation results,
191 chiefly including: the influence of meteorological initial and boundary conditions, underlying
192 surface (mainly considering the impact of urban and water bodies), near-surface layer (N-SL)
193 scheme (the PBL and N-SL schemes must match each other), the effect of model version update,
194 the influence of regional horizontal and vertical resolution, etc. We hope that we can dissect the
195 effect of uncertainties from some aspects that we are concerned about.

196 2 Data and methods

197 2.1 Data

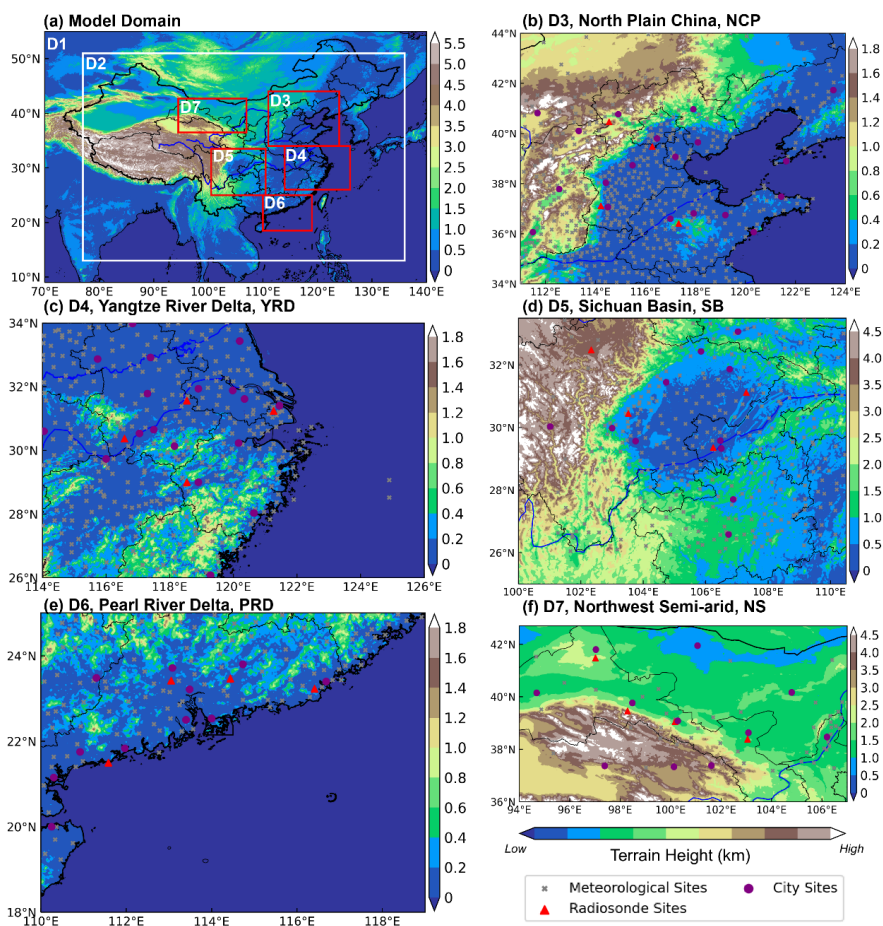
198 **Hourly meteorological observation data.** The China Meteorological Administration (CMA) has
199 over 2400 automatic weather stations (AWSs), and the stations record variables such as temperature,
200 relative humidity, pressure, wind speed, wind direction and precipitation amount. In the NCP, YRD,
201 SB, PRD, NS regions, 576 stations, 455 stations, 341 stations, 128 stations, and 55 stations have
202 been selected, respectively (illustrated by gray cross in Fig. 1b-f). Observational data for four
203 months January, April, July and October 2016 have been selected and comparatively analyzed.
204 **L-band radiosonde observation data.** A total of 120 observation stations are equipped with L-band
205 radiosonde systems in China, which provide fine-resolution (1 Hz, and the rise rate is $\sim 6 \text{ m s}^{-1}$)
206 vertical profiles of temperature, relative humidity and wind speed and direction three times (08:00,
207 14:00 and 20:00 Beijing Time, BJT) a day (illustrated by red triangle in Fig. 1b-f). Four sounding
208 stations have been selected for each region, including different underlying surface conditions as
209 much as possible. In the NCP region, two plain stations (Beijing and Xingtai) and two mountain



210 stations (Zhangjiakou and Zhangqiu) have been picked. In the YRD region, one station closer to the
211 ocean (Shanghai), two stations with complex underlying surface (Anqing and Quzhou), and one
212 plain station (Nanjing) have been opted. In the SB region, three in-basin stations (Wenjiang,
213 Shapingba and Daxian) and one out-of-basin station (Hongyuan, with an altitude of 3491 m) have
214 been selected. In the PRD region, two plain stations (Qingyuan and Heyuan) and two stations
215 (Yangjiang and Shantou) closer to the ocean have been singled out. In the NS region, along the
216 Qilian mountains, four stations have been chosen, Mazongshan, with an altitude of 1770 m, Jiuquan,
217 with an altitude of 1477 m, Zhangye, with an altitude of 1460 m, and Minqin, with an altitude of
218 1367 m.

219 2.2 Model settings

220 In this study, we adopt the model WRF-ARW (Advanced Research Weather Research and
221 Forecasting) version 3.9.1 to evaluate the performance of PBL schemes. Long-term three-
222 dimensional simulation experiments are conducted in 1 month of each season of 2016 (i.e., January,
223 April, July and October). Seven nested domains (D1, D2, D3, D4, D5, D6 and D7) are defined (Fig.,
224 1a), with horizontal grid spacings of 75 km (74 × 74 grid cells, 9°N -59°N, 61°E -146°E), 15 km
225 (281 × 281 grid cells, 13°N -51°N, 77°E -136°E), 3 km (331 × 331 grid cells, 34°N -44°N, 111°E
226 -124°E), 3 km (316 × 356 grid cells, 26°N -34°N, 114°E -126°E), 3 km (331 × 331 grid cells, 25°
227 N -33.5°N, 100°E -110°E), 3 km (236 × 301 grid cells, 18°N -25°N, 110°E -119°E), and 3 km (226
228 × 351 grid cells, 36°N -42.7°N, 94°E -107°E), respectively. Along the vertical direction, 48 vertical
229 layers are configured below the top, and the model top is set to the 50 hPa. To resolve the PBL
230 structure finely, 21 vertical layers are set below 2 km (i.e., the specific setting of vertical levels is σ
231 = 1.000, 0.997, 0.994, 0.991, 0.988, 0.985, 0.980, 0.975, 0.970, 0.960, 0.950, 0.940, 0.930, 0.920,
232 0.910, 0.895, 0.880, 0.865, 0.850, 0.825, 0.800). The initial and boundary conditions of
233 meteorological fields are set up by using the NCEP Global Forecast System (GFS) Final (FNL)
234 gridded analysis datasets, with a resolution of 1° × 1° (<https://rda.ucar.edu/datasets/ds083.2/>, last
235 access: 4 August, 2022). The Moderate Resolution Imaging Spectroradiometer (MODIS) dataset
236 includes 20 land-use categories (Broxton et al., 2014). The physical parameterization used in the
237 present model is listed in Table 1.



238

239

240

241

242

243

244

Figure 1. (a) Map of terrain height in the seven nested model domains. (b-f) Domain 3-7 correspond to the North Plain China (NCP), the Yangtze River Delta (YRD), the Sichuan Basin (SB), the Pearl River Delta (PRD) and the Northwest Semi-arid (NS), respectively. The locations of surface meteorological stations and sounding stations are marked by the gray crosses, red triangles, respectively. The purple dots indicate the major city sites that are our main focus in each region. Table 1. A brief description of the parameterization scheme in the model.

Namelist option	Description	Input option	Reference
mp_physics	Morrison double-moment scheme	10	(Morrison et al., 2009)
ra_lw_physics	RRTMG scheme	4	(Iacono et al., 2008)
ra_sw_physics	RRTMG scheme	4	(Iacono et al., 2008)
cu_physics	Grell-3D scheme	5	(Grell and Dévényi, 2002)
sf_sfclay_physics	MM5 similarity scheme	1	(Jiménez and Dudhia, 2012)
sf_surface_physics	Noah land surface scheme	2	(Chen and Dudhia, 2001)
sf_urban_physics	Single-layer UCM	1	(Kusaka et al., 2001)



	scheme		
sf_lake_physics	CLM4.5 lake scheme	1	(Gu et al., 2015)
	YSU scheme	1	(Hong et al., 2006)
bl_pbl_physics	MYJ scheme	2	(Mellor and Yamada, 1982)
	ACM2 scheme	7	(Pleim, 2007)
	BL scheme	8	(Bougeault and Lacarrere, 1989)

245 All simulations embodied a total of 16 months. The 40 h simulation is conducted beginning from
 246 00:00 UTC of 1d ago for each day (i.e., 492 simulation experiments), the first 16 h of each
 247 simulation is considered as the spin-up period, and results obtained from the following 24 h
 248 simulations are analyzed for the present study.

249 2.3 Description of PBL parameterization schemes

250 2.3.1 YSU scheme

251 The YSU is a first-order nonlocal scheme with an explicit treatment entrainment process at the top
 252 of the PBL:

$$253 \frac{\partial c}{\partial t} = \frac{\partial}{\partial z} \left[K_c \left(\frac{\partial c}{\partial z} - \gamma_c \right) - \overline{(w'c')}_h \left(\frac{z}{h} \right)^3 \right] \quad (1)$$

254 where c denotes u, v, θ , and the $\gamma_c = b \frac{\overline{(w'c')}_0}{w_{s0}h}$ is the counter-gradient flux term, which increases
 255 the nonlocal effect due to the large scale turbulence. z and h are the height of a level of the model
 256 and PBLH, respectively. The PBLH is defined by the bulk Richardson number method:

$$257 h = Rib_{cr} \frac{\theta_{va}|U(h)|^2}{g(\theta_v(h) - \theta_s)} \quad (2)$$

258 where g is the gravity, and Rib is the critical bulk Richardson number, with a value of 0.25 under
 259 stable conditions and 0 under unstable conditions. θ_{va} is the virtual potential temperature at the
 260 lowest model level, $\theta_v(h)$ is the virtual potential temperature at h , θ_s is the appropriate
 261 temperature near the surface ($\theta_s = \theta_{va} + \theta_T$, θ_T is the virtual temperature increment). Compared
 262 to the predecessor of the YSU scheme, the entrainment process is additionally treated explicitly (i.e.,
 263 the last term on the right side of the Eq. (1))

264 Another key variable is K_c , which is the turbulent diffusion coefficient (TDC), and can be
 265 expressed based on the Monin-Obukhov similarity theory (MOST) as:

$$266 K_c = \frac{\kappa u_* z}{\phi_c} \left(1 - \frac{z}{h} \right)^2 \quad (3)$$

267 where u_* is the surface frictional velocity and ϕ_c is dimensionless function, the expressions for
 268 different stability conditions are:

269 i. Unstable and neutral conditions:



270 $\phi_m = \left(1 - 16 \frac{0.1h}{L}\right)^{-1/4}$ (4a)

271 $\phi_h = \left(1 - 16 \frac{0.1h}{L}\right)^{-1/2}$ (4b)

272 ii. Stable condition:

273 $\phi_m = \phi_h = \left(1 + 5 \frac{0.1h}{L}\right)$ (4c)

274 The TDC of momentum (i.e., K_m) is first calculated in the model, and then the TDC of heat (i.e.,

275 K_h) is calculated, using the Prandtl number (i.e., $Pr = \frac{K_m}{K_h}$). The TDC controls the vertical mixing

276 process of momentum and scalars within the PBL, and it is crucial that it needs to be accurately

277 described.

278 **2.3.2 MYJ scheme**

279 The MYJ scheme is a one-and-a-half order local closure scheme with a prognostic equation for

280 turbulent kinetic energy (TKE, $TKE = e = \frac{1}{2}(u'^2 + v'^2 + w'^2)$):

281 $\frac{\partial \bar{e}}{\partial t} = -\frac{1}{\bar{\rho}} \frac{\partial}{\partial z} \overline{w'p'} - \overline{w'u'} \frac{\partial \bar{u}}{\partial z} - \overline{w'v'} \frac{\partial \bar{v}}{\partial z} - \frac{\partial}{\partial z} \overline{w'e'} + \frac{g}{\theta_v} \overline{w'\theta'_v} - \varepsilon$ (5)

282 The first term on the right side of Eq. (5) is a pressure correlation term which describes TKE is

283 redistributed by pressure perturbations, the second and third terms is a shear production/loss term,

284 the fourth term represents the turbulent transport of TKE, the fifth term describes the buoyant

285 production/consumption term, and the sixth term represents viscous dissipation of TKE. To close

286 the TKE equation, the turbulent fluxes must be parameterized. Based on the gradient transport

287 theory (i.e., K-theory), the turbulent fluxes can be indicated as:

288 $\overline{w'u'} = -K_m \frac{\partial \bar{u}}{\partial z}$ (6a)

289 $\overline{w'v'} = -K_m \frac{\partial \bar{v}}{\partial z}$ (6b)

290 $\overline{w'\theta'_v} = -K_h \frac{\partial \bar{\theta}}{\partial z}$ (6c)

291 The TDC is proportional to the square root of TKE, and can be expressed as:

292 $K_m = S_m l e^{1/2}$ (7a)

293 $K_h = S_h l e^{1/2}$ (7b)

294 where l is mixing length and can be described as $l = \frac{l_0 \kappa z}{\kappa z + l_0}$, where $l_0 = \alpha \int_0^\infty z e^{1/2} dz$, α is an

295 empirical constant (=0.1). When z converges to a very small value, l converges to κz . However, as

296 z converges to a very large value, l converges to l_0 .

297 To obtain the S_m and S_h in Eq. (7), G_m and G_h are defined as:



298 $G_m = \frac{l^2}{ze} \left[\left(\frac{\partial \bar{u}}{\partial z} \right)^2 + \left(\frac{\partial \bar{v}}{\partial z} \right)^2 \right] \quad (8a)$

299 $G_h = -\frac{l^2 g}{ze \theta_v} \frac{\partial \theta_v}{\partial z} \quad (8b)$

300 S_m and S_h are functions of G_m and G_h , and can be denoted as:

301 $S_m(6A_1A_2G_m) + S_h(1 - 3A_2B_2G_h - 12A_1A_2G_h) = A_2 \quad (9a)$

302 $A_1(1 + 6A_1^2G_m - 9A_1A_2G_h) - S_h(12A_1^2G_h + 9A_1A_2G_h) = A_1(1 - 3C_1) \quad (9b)$

303 where $[A_1, A_2, B_1, B_2, C_1] = [0.660, 0.657, 11.878, 7.227, 0.001]$.

304 The PBLH in the MYJ scheme is defined as the height at which the TKE is reduced to a critical
 305 value of $0.1 \text{ m}^2 \text{ s}^{-2}$.

306 2.3.3 ACM2 scheme

307 Unlike the YSU scheme, the ACM2 scheme applies the transilient matrix to deal with the
 308 contribution of nonlocal fluxes. The governing equation can be expressed as:

309 $\frac{\partial C_i}{\partial t} = f_{conv} Mu C_1 - f_{conv} Md_i C_i + f_{conv} Md_{i+1} C_{i+1} \frac{\Delta z_{i+1}}{\Delta z_i} + \frac{\partial}{\partial z} \left[K_c (1 - f_{conv}) \frac{\partial C_i}{\partial z} \right] \quad (10)$

310 The first three terms on the right side of Eq. (10) represent nonlocal mixing effect and the fourth
 311 term represents local mixing effect. Where C_i is the variable at layer i , Mu is the nonlocal upward
 312 convective mixing rate, Md_i is the downward mixing rate from layer i to layer $i-1$, Δz_i is the
 313 thickness of layer i , and C_1 represents the variable at the lowest layer in the model. f_{conv} is the
 314 weighting factor for the nonlocal and local effects (i.e., $f_{conv} = \frac{K_h \gamma_h}{K_h \gamma_h - K_h \frac{\partial \theta}{\partial z}}$), where the value of f_{conv}

315 ranges from 0 to 1, a larger f_{conv} indicates stronger nonlocal mixing.

316 There are two methods to calculate the TDC, and the first method is the same as the YSU scheme,
 317 i.e., Eq. (3), but there is also a very stable condition in the ACM2 scheme. In this case, the
 318 dimensionless function can be expressed as $\phi_m = \phi_h = \left(5 + \frac{0.1h}{L} \right)$.

319 The second calculation principle is based on the mixing length theory, which uses mixing length
 320 and stability function to calculate TDC:

321 $K_h = 0.01 + l^2 \sqrt{ss} f_h(Ri) \quad (11)$

322 where l is similar to the MYJ scheme, but l_0 is a constant (=80), ss is the wind shear ($ss =$
 323 $(\partial \bar{u} / \partial z)^2 + (\partial \bar{v} / \partial z)^2$), 0.01 denotes the minimum value of the TDC in the model, and $f_h(Ri)$ is
 324 the empirical stability functions of gradient Richardson number of heat.

325 i. when $Ri \geq 0$:

326 $f_h(Ri) = (1 - 25Ri)^{1/2} \quad (12a)$

327 ii. when $Ri < 0$:

328 $f_h(Ri) = \frac{1}{1 + 10Ri + 50Ri^2 + 5000Ri^4} + 0.0012 \quad (12b)$



329 Similarly, the empirical stability functions of momentum can be indicated as:

330 i. when $Ri < 0$:

331 $f_m(Ri) = Pr \cdot f_h(Ri) + 0.00104$ (13a)

332 $K_m = 0.01 + l^2 \sqrt{ss} f_m(Ri)$ (13b)

333 ii. when $Ri \geq 0$:

334 $K_m = Pr \cdot K_h$ (13c)

335 The ACM2 scheme has a range setting for the TDC in the model with a minimum value of 0.01 m²
 336 s⁻² and a maximum value that cannot exceed 1000 m² s⁻².

337 The PBLH discrimination in the ACM2 scheme is similar to the YSU scheme, and is defined with
 338 the bulk Richardson number method. The difference is that the entrainment region at the top of the
 339 PBL is considered in the ACM2 scheme, and turbulence still exists due to the wind shear and thermal
 340 penetration. Therefore, special processing of the PBLH is required under unstable and stable
 341 conditions.

342 2.3.4 BL scheme

343 The BL scheme is also a one-and-a-half order local closure scheme, and the TDC is calculated in a
 344 similar way to Eq. (7) of the MYJ scheme. Nevertheless, the function S_m and mixing length (i.e., l)
 345 are different from the MYJ scheme. In the BL scheme, S_m is a constant 0.4 and the l is divided into
 346 upward and downward mixing length (i.e., l_{up} and l_{down}), which are defined as:

347 $\int_z^{z+l_{up}} \beta[\theta(z) - \theta(z')] dz' = e(z)$ (14a)

348 $\int_{z-l_{down}}^z \beta[\theta(z') - \theta(z)] dz' = e(z)$ (14b)

349 where, β is the buoyancy coefficient and the l is equal to the minimum of l_{up} and l_{down} (i.e., $l =$
 350 $\min(l_{up}, l_{down})$). It is worth noting that in the BL scheme the TDC of heat is equal to the TDC of

351 momentum (i.e., $K_h = K_m$). In addition, the PBLH of the BL scheme is defined as the height at which
 352 the virtual potential temperature of a layer is greater than that of the first layer by 0.5 K.

353 To accommodate different methods of calculating PBLH for different schemes and to evaluate the
 354 simulation performance of PBLH, two methods are employed to calculate PBLH using observed
 355 data in this study, the first being the bulk Richardson number method, and the detailed calculation
 356 principle is as follows (Miao et al., 2018):

357 $Ri(z) = \frac{(g/\theta_s)(\theta_z - \theta_s)(z - z_s)}{(u_z - u_s)^2 + (v_z - v_s)^2 + bu_s^2}$ (15)

358 here z is the height, g is the gravity, θ is the virtual potential temperature, u and v are the components
 359 of the horizontal wind, b is a constant, and u_* is the friction velocity. The subscript “s” indicates
 360 the near-surface. Since the friction velocity is much smaller in magnitude than the wind shear, the
 361 b is set to 0, ignoring the effect of surface friction (Vogelezang and Holtslag, 1996; Seidel et al.,
 362 2012). The PBLH is estimated as the lowest layer height when Ri reaches a critical value of 0.25.



363 The second method adopts the same calculation method as the BL scheme, i.e., the virtual potential
364 temperature method:

$$365 \Delta\theta_{v|PBLH} = \theta_{v1} + 0.5 \quad (16)$$

366 The PBLH is the height when the virtual potential temperature exceeds the virtual potential
367 temperature of the first level by 0.5 K.

368 2.4 Evaluation of the model

369 To evaluate the PBL schemes and the performance of the model for estimating meteorological
370 variables, the statistical parameters used in this statistical analysis are defined as follows (Emery et
371 al., 2017):

372 Index of agreement (IOA):

$$373 IOA = 1 - \frac{[\sum_{i=1}^n |X_{sim,i} - X_{obs,i}|^2]}{[\sum_{i=1}^n (|X_{sim,i} - \bar{X}_{obs}| + |X_{obs,i} - \bar{X}_{obs}|)^2]} \quad (17)$$

374 Mean bias (MB):

$$375 MB = \frac{1}{n} \sum_{i=1}^n (X_{sim,i} - X_{obs,i}) \quad (18)$$

376 Root mean square error (RMSE):

$$377 RMSE = \sqrt{\frac{1}{n} \sum_{i=1}^n (X_{sim,i} - X_{obs,i})^2} \quad (19)$$

378 Normalized standard deviations (NSD):

$$379 NSD = \frac{\sqrt{\frac{1}{n-1} \sum_{i=1}^n (X_{sim,i} - \bar{X}_{sim})^2}}{\sqrt{\frac{1}{n-1} \sum_{i=1}^n (X_{obs,i} - \bar{X}_{obs})^2}} \quad (20)$$

380 Relative bias (RB):

$$381 RB = \frac{\bar{X}_{sim} - \bar{X}_{obs}}{\bar{X}_{obs}} \times 100\% \quad (21)$$

382 Where $X_{sim,i}$ and $X_{obs,i}$ represent the value of simulation and observation, respectively, i refers
383 to time and n is the total number of time series. \bar{X}_{sim} and \bar{X}_{obs} represent the average simulation
384 and observation.

385 The Taylor diagram is a compact tool that displays simultaneously the values of four statistical
386 parameters: IOA, NSD, RB, and RMSE. In particular, in these diagrams the perfect match of a
387 model with the observations would be the point with IOA=1, NSD=1, RB=0 and RMSE=0.

388 3 Results and discussion

389 In section 3.1, the mechanistic analysis of the PBL schemes for the simulation of near-surface
390 meteorological parameters, including 2-m temperature, 2-m relative humidity, 10-m wind speed and
391 direction. Section 3.2 gives an in-depth analysis of different schemes for PBL vertical structure. In
392 section 3.3, the PBLH was evaluated for different schemes. In section 3.4, the reason for the

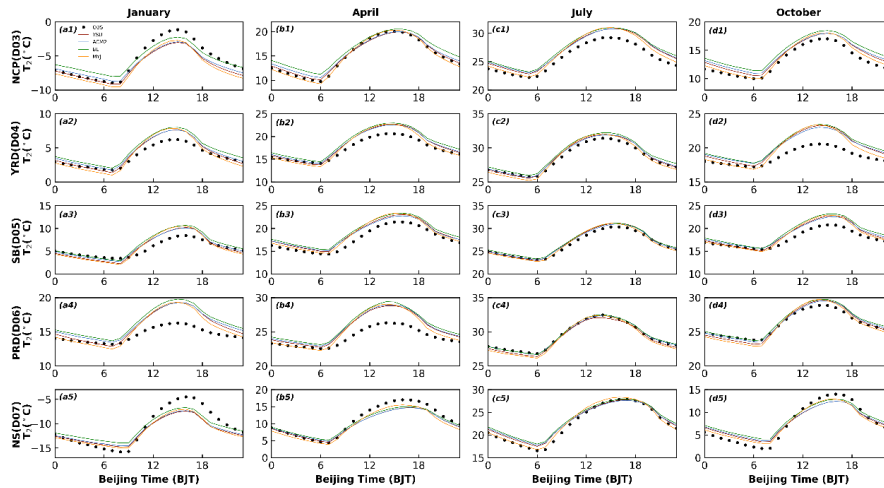


393 differences in turbulent diffusion are interrogated from the calculation principle of the schemes.
394 Section 3.5 summarizes the performance and expressiveness of different PBL schemes in different
395 regions, and recommends the optimal choice of PBL scheme.

396 3.1 surface meteorological variables

397 3.1.1 2-m temperature and relative humidity

398 To better analyze the variation of the time series, we selected representative stations in different
399 regions. Figure 2 shows the diurnal variation of 2-m temperature (i.e., T_2) for four months (i.e.,
400 January, April, July and October 2016) at representative sites (indicated in the orange dots in Fig. 1)
401 in the five regions. The model basically captures the daily variation characteristics of T_2 , but there
402 are significant differences between different regions and seasons. The simulated results for July are
403 closest to the observed values (Fig. 2 c1-c5), anywhere. Overall, the mean biases (MBs) of the
404 diurnal variation of T_2 predicted in July for the NCP, YRD, SB, PRD and NS regions are 0.61~1.19,
405 -0.02~-0.56, -0.32~-0.60, -0.38~-0.69, and 0.28~0.81 °C, respectively. However, a smaller value of
406 the mean bias does not mean that the simulated value of the model is closer to the observed value.
407 For example, if one overestimation and the other underestimation occur during the day and night,
408 the average results will cancel each other out, resulting in a small mean bias. Accordingly, more
409 statistical parameters are needed to further evaluate the optimal scheme. In the other three months
410 (January, April, and October), the simulated results of T_2 are overestimated to varying degrees
411 during daytime in the YRD, SB and PRD regions, while in the NS region, T_2 are underestimated to
412 varying degrees (Fig. 2 a2-b5, d2-d5 and Table 1). In the NCP regions, T_2 presents underestimation
413 in January by the model with the YSU, ACM2, BL and MYJ schemes are -1.33, -1.21, -0.52 and -
414 1.18 °C, respectively, while overestimation arises in the other three months (Table 1). In the five
415 regions, the simulation results of the nighttime T_2 outperform those of the daytime T_2 for almost
416 four months. At night, the MYJ scheme shows a significant underestimation of T_2 for all months in
417 five regions compared to the other three schemes (Fig. 2 and Table 1). The simulation results of Hu
418 et al. (2010) and Xie et al. (2012) have also obtained the lowest temperature for the MYJ scheme
419 during the nighttime.



420
 421 **Figure 2. Time series of diurnal variation of observed and simulated 2-m temperature in five**
 422 **regions for four seasons.**

423 The 2-m temperature does not actually represent the air temperature at a height of 2 m, but it is a
 424 diagnostic variable of the near-surface temperature. It is calculated from the surface temperature
 425 (T_s), the sensible heat flux (HFX) and the heat transfer coefficient (C_h). The T_s is a prognostic
 426 variable, which is obtained in the model through the energy balance equation:

427
$$(1 - \alpha)S \downarrow + L \downarrow - L \uparrow + G - HFX - LH = 0 \quad (22)$$

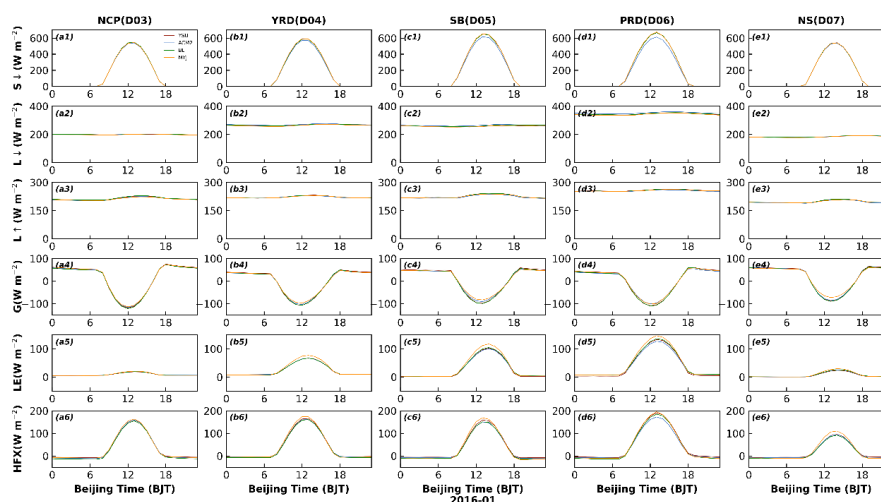
428 where α is the albedo of the underlying surface, $S \downarrow$ represents the downward of the shortwave
 429 radiation, $L \downarrow$ is the downward of the longwave radiation emitted by the cloud and atmosphere,
 430 $L \uparrow$ is the upward of the longwave emitted by the ground surface, G is the ground heat flux, and it
 431 is positive when heat transfers from the soil to the near surface, HFX is the sensible heat flux and
 432 LH is the latent heat flux.

433 We compare the effects of the six variables mentioned above on T_s with the expectation that we can
 434 further examine the reasons for the differences in T_2 variation between different schemes. The YSU
 435 scheme is used as a control and analyzed in comparison with each of the schemes.

436 The nonlocal closure scheme (YSU) and the local closure scheme (MYJ) are compared first.
 437 Theoretically, the greater the downward shortwave radiation ($S \downarrow$) becomes, the more energy reaches
 438 the ground, and the higher the surface temperature (T_s) is. After comparing the YSU and MYJ
 439 schemes, the surface temperature does not show a proportional change with the downward
 440 shortwave radiation, and the $S \downarrow$ of the MYJ scheme is almost the same as that of the YSU scheme
 441 (Fig. 3 a1-e1), but the T_s of the MYJ scheme is the lowest (Fig. 4 a1-e1). Therefore, the $S \downarrow$ is not
 442 the main factor that causes the difference in T_s between the two schemes. There is no significant
 443 difference in the upward/downward longwave radiation between these two schemes (Fig. 3 a2-e3),
 444 so the effect of longwave radiation on the T_s can also be excluded. During the daytime, the MYJ



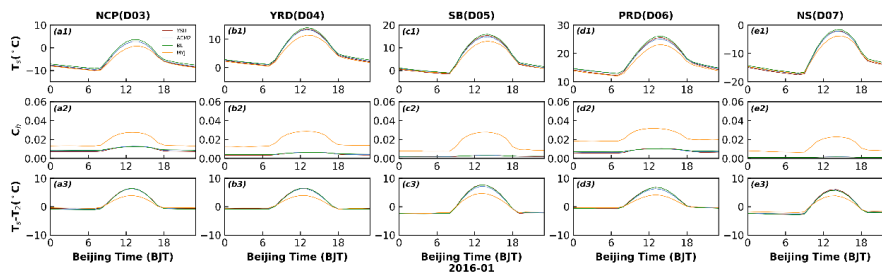
445 scheme transfers less heat from the surface to the soil than the YSU scheme (Fig. 3 a4-e4), and the
 446 T_s of the MYJ scheme should be higher than that of the YSU scheme. But that's not how it has
 447 turned out (Fig. 4 a1-e1). Thus, the ground heat flux (G) is also not a key factor that directly affects
 448 the T_s . The latent heat flux (LH) is mainly related to water vapor (or relative humidity), so further
 449 attention is paid to the effect of sensible heat flux (HFX) on T_s (Fig. 3 a5-e6). The HFX is determined
 450 by the difference between the surface temperature and the 2-m temperature ($T_s - T_2$), and the heat
 451 transfer coefficient (C_h). MYJ has the largest HFX, and transfers more heat from the surface to the
 452 atmosphere, resulting in the largest energy loss at the surface, which should correspond to the
 453 smallest T_s (Fig. 3 a6-e6, 4 a1-e1). The smallest difference between the two temperatures indicates
 454 a smaller temperature gradient and more uniform mixing, symbolizing the largest C_h , which is also
 455 true (Fig. 4 a2-e3). A larger C_h would lead to higher T_2 during the day. Although the T_s of the MYJ
 456 scheme is significantly lower than YSU scheme, it makes the T_2 higher due to the large C_h . During
 457 the daytime, the less heat is transferred from the surface to the soil in the MYJ scheme, which results
 458 in lower soil temperature. During the nighttime, the difference in HFX and temperature gradient
 459 between the two schemes decreases, and the lower soil temperature results in lower T_s and T_2 .



460
 461 **Figure 3.** Time series of diurnal variation of (a1-e1) downward shortwave radiation ($S \downarrow$), (a2-e2)
 462 downward longwave radiation ($L \downarrow$), (a3-e3) upward longwave radiation ($L \uparrow$), (a4-e4) ground heat
 463 flux (G), (a5-e5) latent heat flux (LH), and (a6-e6) sensible heat flux (HFX) by four PBL schemes
 464 in five regions in January.
 465 The differences between the YSU scheme and the ACM2 scheme are further explored. Except for
 466 the NCP and NS regions, the $S \downarrow$ of the ACM2 scheme is smaller than that of the YSU scheme in
 467 the other three regions (i.e., YRD, SB and PRD) (Fig. 3 b1-d1). The HFX of the ACM2 scheme is
 468 smaller than that of the YSU scheme (Fig. 3 b6-d6), the heat loss from the surface of the ACM2



469 scheme is less, and the T_s of the ACM2 scheme should be higher. However, the T_s corresponding to
 470 the ACM2 scheme is lower than that of the YSU scheme (Fig. 4 b1-d1), reflecting that the $S \downarrow$
 471 varies proportionally with the T_s , and it is the main factor controlling the T_s variation. In the ideal
 472 case, assuming the same temperature gradient for the nonlocal schemes, the T_2 of the YSU scheme
 473 should also be higher than that of the ACM2 scheme when the T_s of the YSU scheme is higher than
 474 that of the ACM2 scheme with the same C_h . But in fact, it can be seen that the C_h of the ACM2
 475 scheme and YSU scheme are the same (Fig. 4 b2-d2), and the temperature gradient of the YSU
 476 scheme is greater than that of ACM2 scheme (Fig. 4 b3-d3). The T_2 of the ACM2 scheme should be
 477 slightly higher than the ideal case, closer to the T_2 of the YSU scheme, and even may also exceed
 478 T_2 of the YSU scheme. At night, the T_s of the YSU scheme is lower than that of the ACM2 scheme,
 479 and the C_h of the YSU scheme is smaller than that of the ACM2 scheme (Fig. 4 a1-e2). Meanwhile,
 480 the difference in HFX between the two schemes is not obvious at night, contributing to lower T_2 of
 481 the YSU scheme. In both NCP and NS regions, there is no significant difference in downward
 482 shortwave radiation between two schemes, and no noticeable difference between T_2 and T_s .



483
 484 **Figure 4. Time series of diurnal variation of (a1-e1) surface temperature (T_s), (a2-e2) heat transfer**
 485 **coefficient (C_h) and (a3-e3) the difference between the surface temperature and the 2-m**
 486 **temperature (T_s-T_2) by four PBL schemes in five regions in January (Winter).**

487 Then, the reasons for the simulated temperature difference between the YSU scheme and the BL
 488 scheme are demonstrated. During the daytime, the $S \downarrow$ of both schemes are the same (Fig. 3 a1-e1),
 489 but the HFX of the BL scheme is smaller than that of the YSU scheme (Fig. 3 a6-e6), less heat is
 490 loss at the surface, hence the T_s should be higher than that of the YSU scheme (Fig. 4 a1-e1). The
 491 C_h of both schemes are the same, thus, the BL scheme has a higher T_2 (Fig. 2, 4a1-e2). At night, the
 492 HFX of BL scheme is larger than that of YSU scheme, and more heat is transferred from atmosphere
 493 to the surface, and the larger C_h resulting in higher T_2 (Fig. 3 a6-e6, 4 a1-e2).

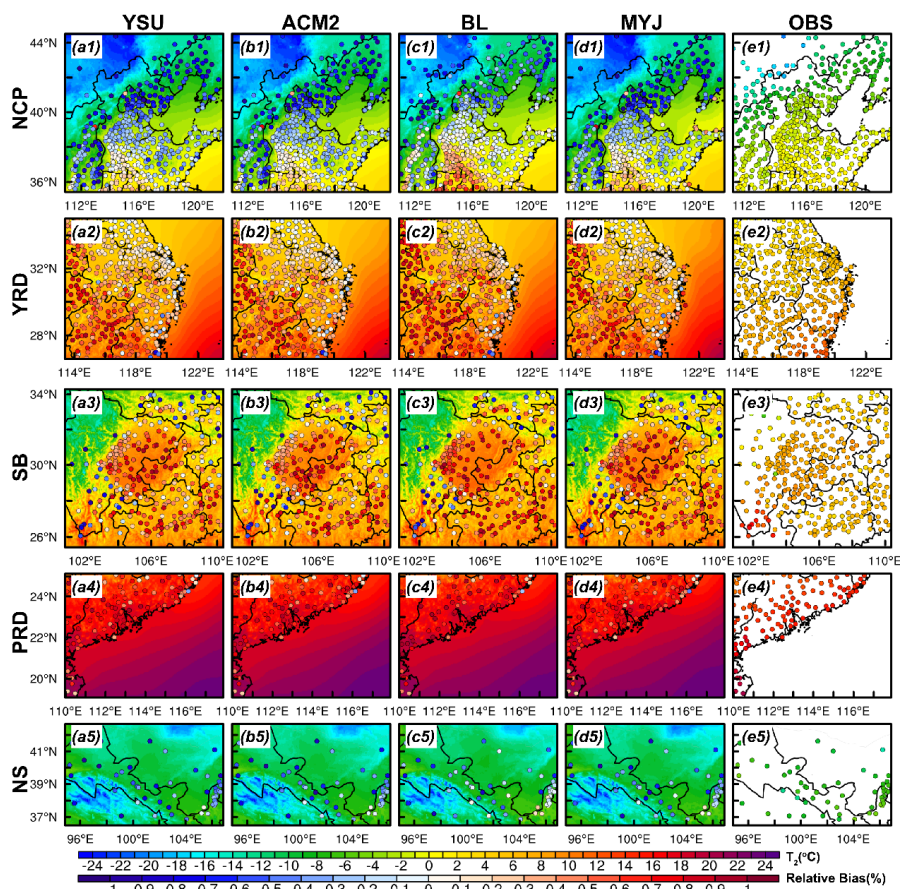
494 Finally, we can also uncover the reasons for the difference between the local closure schemes (MYJ
 495 and BL). The larger HFX of the MYJ scheme leads to a lower T_s in the daytime, while the
 496 temperature gradient of MYJ scheme is smaller than that of the BL scheme, and C_h is larger than
 497 BL scheme (Fig. 3 a6-e6, 4). Therefore, the difference in T_2 between the two schemes is smaller
 498 than that in T_s . The T_2 of the MYJ scheme is closer to that of the BL scheme.



499 In conclusion, the causes of temperature differences simulated by the nonlocal closure schemes
500 should first focus on the effect of the downward shortwave radiation (S_{\downarrow}), and when it comes to the
501 local closure scheme, the effect of HFX should be further concerned. All of the above results have
502 been analyzed for January 2016, and the results for the other three months are similar (Figs. S1-S6).
503 In terms of regional distribution differences, T_2 in the northern and near mountainous regions of the
504 NCP region is significantly underestimated in the daytime for January, April and October, while T_2
505 in other regions shows an overestimation (Fig. 5, S7, S8 a1-e1). The range of overestimated areas
506 is smaller than the underestimated in January, only in a small part of the area south of Hebei Province
507 (Fig. 5 a1-e1). The relative bias (RB) of the underestimated (overestimated) T_2 with the YSU, ACM2,
508 BL and MYJ schemes are -0.60% (0.15%), -0.57% (0.17%), -0.43% (0.26%) and -0.60% (0.20%),
509 respectively in January. Also in these three months, temperature is overestimated at almost all
510 stations in the YRD region (RB=0.38%~0.50% in January, RB=0.49%~0.65% in April and
511 RB=0.58%~0.70% in October) and underestimated at some stations along the coast (RB=-0.13%~
512 0.24% in January, RB=-0.32%~0.37% in April and RB=-0.23%~0.28% in October) (Fig. 5, S7,
513 S8 a2-e2). The results show an overestimation of T_2 simulated in those stations in the basin for the
514 SB region as well as the simulation results of the stations in the plain for the NCP region, while for
515 the stations in the hilltop areas, the T_2 shows an underestimation (Fig. 5, S7, S8 a3-e3). In the PRD
516 region, the entire region exhibits an overestimation of T_2 , with the simulation results in October
517 (RB=0.06%~0.15%) being significantly better than those in January (RB=0.59%~0.81%) and April
518 (RB=0.56%~0.67%), with a lower degree of T_2 overestimation (Fig. 5, S7, S8 a4-e4). The BL
519 scheme simulates a higher T_2 and a large range of overestimated areas (about 167, 378, 252 and 100
520 stations in NCP, YRD, SB and PRD regions). The NS region has a more complex topography and
521 higher elevation, and the T_2 is underestimated at almost all stations, with best simulation results in
522 October (RB=-0.04%~0.21%) and worst in April (RB=-0.49%~0.64%).
523 For July, when the temperature is higher, the simulation results are significantly different from the
524 other three months. The relative bias of T_2 simulated with the YSU, ACM2, BL and MYJ schemes
525 are 0.47%, 0.46%, 0.53% and 0.46%, respectively, in the NCP region. The overestimation results
526 are similar to daytime, with the most pronounced overestimation for the BL scheme. For the
527 southern region of the NCP, the T_2 is consistently overestimated regardless of the season (Fig. S9
528 a1-e1). The T_2 at most stations are underestimated in the YRD region, which is different from the
529 other three months (Fig. S9 a2-e2). In summer, the temperature of the ocean, affected by the
530 subtropical high (prevailing southeasterly winds), is lower than that of the land, and the transport of
531 momentum is accompanied by the transport of heat from the sea to the land, causing the temperature
532 of the land to decrease. The T_2 of the basin area in the SB region is well reproduced, and no
533 significant overestimation occurs (Fig. S9 a3-e3). There is an underestimation of the T_2 at most
534 stations in the PRD region, but to a lesser extent (Fig. S9 a4-e4). In contrast, for the NS region, the



535 temperature is overestimated for areas at lower elevations, while underestimated (or better
 536 reproduced) for areas at higher elevations (Fig. S9 a5-e5).

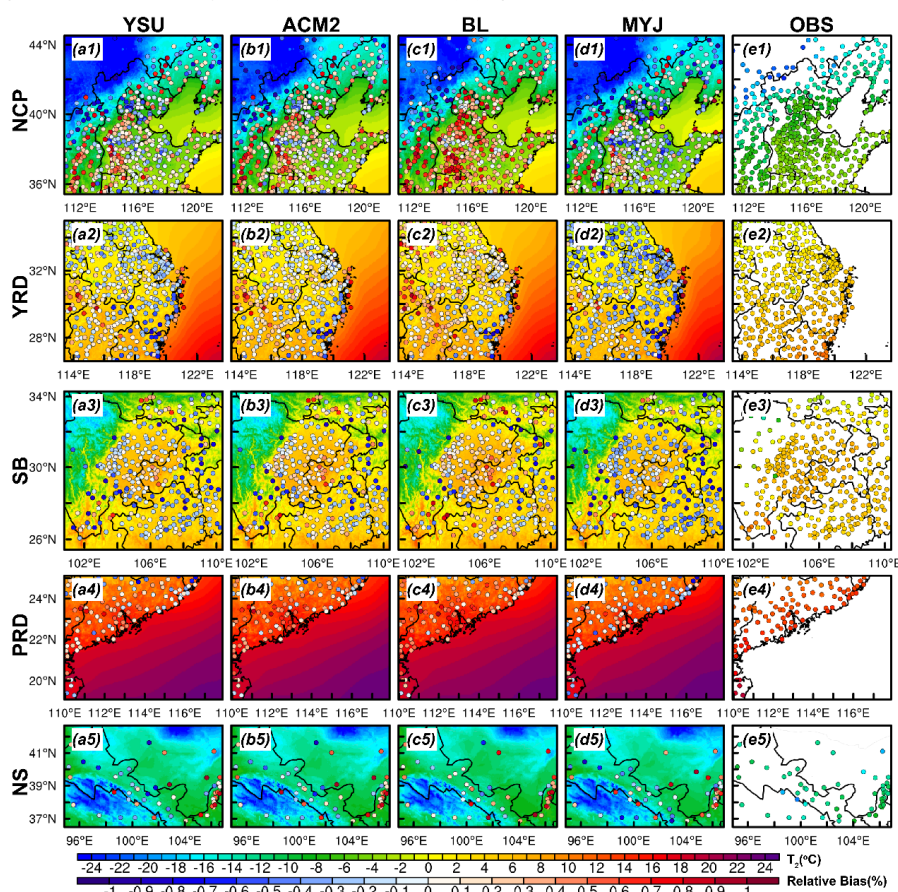


537
 538 **Figure 5.** Regional distribution of 2-m temperature simulated by (a-d) four PBL schemes in five
 539 regions during the daytime in January (Winter), (e1-e5) distribution of observation in five regions,
 540 and (a1-d5) distribution of relative bias between simulations and observations is denoted by
 541 scatters.

542 The relative deviation of the nighttime T_2 simulations is less than that of the daytime, regardless of
 543 the region and month (Fig. 6, S10-S12). The differences between the four schemes are more striking
 544 at night compared to the daytime. The BL scheme simulates the highest T_2 and the MYJ scheme
 545 simulates the lowest T_2 in the whole region (Fig. 6, S10-S12). Compared to the observed values, the
 546 MYJ scheme is the best when all schemes overestimate the simulated temperature, but if there is an
 547 underestimation, the MYJ scheme is no longer the best scheme. Later, a comprehensive statistical
 548 evaluation of the schemes will be presented. For the NCP region, the overestimation and
 549 underestimation in the whole region do not show a north-south divide (or a mountain-plain divide)



550 as in the daytime (Fig. 5, 6 a1-e1). In the YRD region, the temperature along the coastal area still
 551 shows a significant underestimation (Fig. 6, S10-S12 a2-e2). Similar to the daytime, the temperature
 552 at stations in the hill top areas of the SB region still presents an underestimation (Fig. 6, S10-S12
 553 a3-e3). Most stations show the underestimation of T_2 in July and October in the PRD region (Fig.
 554 S11-S12 a4-e4). In the NS region, the relative deviation of temperature simulations in October is
 555 greater than that in daytime (RB=0.17%~0.56%) (Fig. 5, S12 a5-e5).

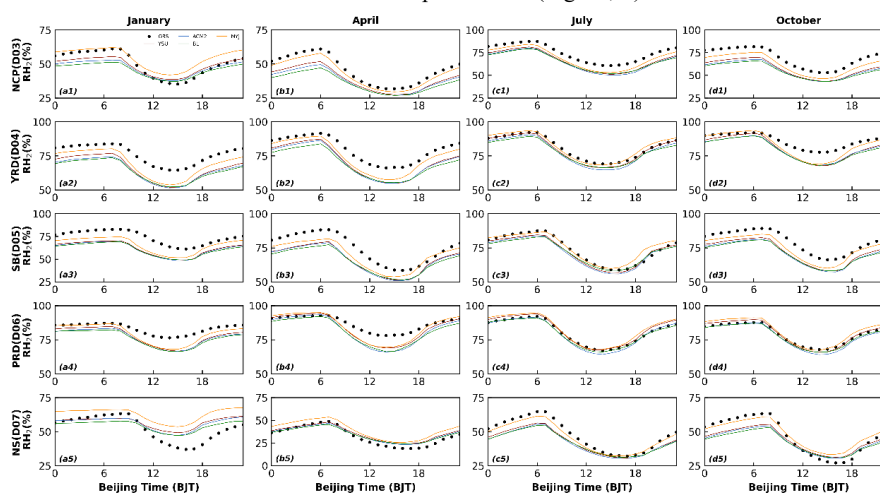


556
 557 **Figure 6. Similar as Figure 5, but at night.**

558 In summary, the simulation results of T_2 have the following main characteristics. From the
 559 perspective of differences between observations and simulations, (1) the simulation results for July
 560 are better compared to the other three months. (2) The simulation results at night are better than
 561 those at daytime, with less relative deviation. (3) The temperature is easily underestimated at higher
 562 altitudes while overestimated in plains and basin areas. From the perspective of the differences
 563 between the different schemes, (1) the differences in the performance of the four schemes are more
 564 noticeable at night. (2) The difference in the simulation of temperature in the nonlocal closure



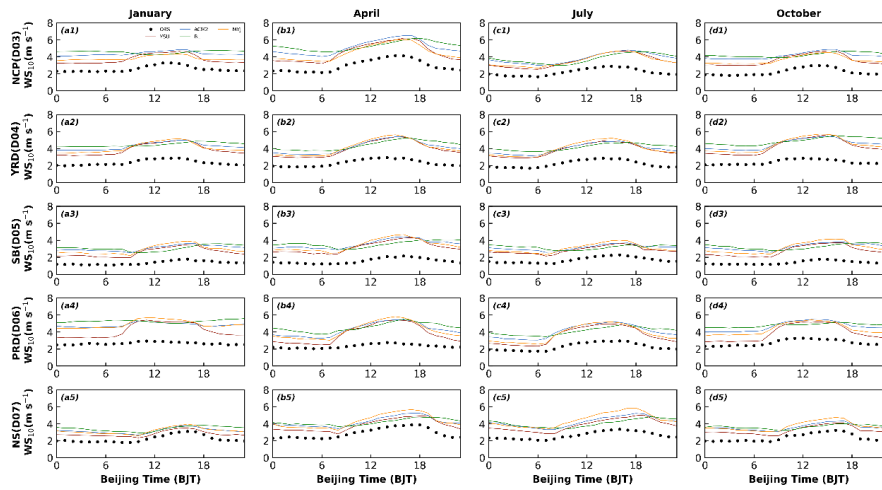
565 schemes is mainly attributed to the difference in downward shortwave radiation ($S \downarrow$), and the
 566 difference in the variation of sensible heat flux (HFX) needs to be further analyzed when the local
 567 closure schemes are involved. (3) The BL scheme simulates the highest temperature and the MYJ
 568 scheme for the lowest temperature.
 569 The results for 2-m relative humidity (RH₂) and T₂ correspond to each other, and the overestimation
 570 of T₂ corresponds to the underestimation of RH₂. The simulation of RH₂ still shows the best results
 571 in July, with the highest simulated values for the MYJ scheme and the lowest for the BL scheme.
 572 Except for the NS region, the simulated RH₂ of the other four regions is almost underestimated.
 573 This uniform trend in relative humidity may be due to errors in the initial field, which will be
 574 discussed in Part II. Too much will not be repeated here (Figs. 2, 7).



575
 576 **Figure 7.** Similar as Figure 2, but for 2-m relative humidity.

577 3.1.2 10-m wind speed and direction

578 Although the model simulates the diurnal cycle of wind speed, the wind speed shows different
 579 degrees of overestimation, and the mean bias is in the range of 0.86 m s^{-1} – 2.74 m s^{-1} (Fig. 8, Table
 580 2). This is also the conclusion reached in many previous studies and it is more widely accepted by
 581 the public. Except for the NCP region where the MYJ scheme has the largest mean bias (MB) value
 582 during the day (YSU: MB= 1.6 m s^{-1} , ACM2: MB= 1.8 m s^{-1} , BL: MB= 1.7 m s^{-1} , MYJ: MB= 2.1 m s^{-1}),
 583 while the BL scheme has the largest MB value at night regardless of the region (YSU: MB= 1.3
 584 m s^{-1} , ACM2: MB= 1.8 m s^{-1} , BL: MB= 2.2 m s^{-1} , MYJ: MB= 1.7 m s^{-1}) (Fig. 8, Table 2).



585

586

Figure 8. Similar as Figure 2, but for 10-m wind speed.

587

Table 2. Mean bias of 2-m temperature, 2-m relative humidity and 10-m wind speed during daytime and nighttime by four PBL schemes in five regions and four seasons.

588

Variables	Regions						
	Schemes/Seasons	NCP	YRD	SB	PRD	NS	
T ₂ -Day	YSU	Jan	-1.33	0.91	0.20	1.84	-1.42
		Apr	0.27	1.35	0.77	1.74	-1.83
		Jul	1.41	-0.18	-0.20	-0.66	0.38
		Oct	0.91	1.69	0.68	0.25	-0.58
	ACM2	Jan	-1.21	0.97	0.29	1.93	-1.29
		Apr	0.34	1.28	0.64	1.79	-1.82
		Jul	1.37	-0.21	-0.31	-0.49	0.27
		Oct	0.98	1.54	0.61	0.21	-0.50
	BL	Jan	-0.52	1.33	0.73	2.32	-0.76
		Apr	0.89	1.71	1.07	2.00	-1.43
		Jul	1.60	0.04	-0.16	-0.38	0.55
		Oct	1.49	1.88	1.09	0.46	-0.09
MYJ	Jan	-1.18	0.92	0.32	1.70	-1.23	
	Apr	0.45	1.19	0.87	1.66	-1.39	
	Jul	1.38	-0.29	-0.28	-0.58	0.64	
	Oct	0.83	1.56	0.68	0.18	-0.45	
T ₂ -Night	YSU	Jan	-0.14	-0.27	-0.98	0.15	0.33
		Apr	0.04	-0.17	0.13	0.24	-0.23
		Jul	0.39	-0.53	-0.78	-0.54	0.68
		Oct	0.51	0.06	-0.52	-0.56	1.04
	ACM2	Jan	0.15	0.03	-0.74	0.56	0.52
		Apr	0.47	0.07	0.23	0.39	-0.07
		Jul	0.57	-0.40	-0.72	-0.27	0.86
		Oct	0.86	0.35	-0.29	-0.28	1.24
	BL	Jan	0.88	0.34	-0.45	0.80	1.03
		Apr	1.21	0.48	0.53	0.64	0.23
		Jul	0.79	-0.08	-0.48	-0.21	1.07
		Oct	1.37	0.54	-0.06	-0.04	1.59
MYJ	Jan	-0.46	-0.59	-1.16	-0.28	0.21	
	Apr	-0.70	-0.62	-0.27	-0.19	-0.97	
	Jul	-0.15	-0.83	-0.93	-0.80	-0.08	



		Oct	0.01	-0.34	-0.74	-0.83	0.52
		Jan	-0.01	-9.95	-10.71	-6.62	7.19
	YSU	Apr	-7.09	-7.59	-5.75	-5.02	3.02
		Jul	-8.46	1.18	-0.16	3.18	-5.56
		Oct	-11.07	-5.62	-5.17	0.57	-1.02
	ACM2	Jan	-0.92	-10.77	-11.63	-7.43	6.05
		Apr	-7.82	-8.32	-6.64	-7.12	2.03
		Jul	-9.79	-0.65	-1.71	0.51	-6.18
		Oct	-11.83	-5.93	-6.23	-1.44	-2.09
	BL	Jan	-1.66	-10.53	-11.36	-7.54	5.40
		Apr	-7.89	-8.32	-5.90	-6.31	2.36
		Jul	-8.02	0.68	0.92	1.71	-5.06
		Oct	-12.47	-6.10	-5.67	-0.38	-2.10
	MYJ	Jan	4.47	-6.72	-7.69	-4.74	12.55
		Apr	-4.39	-4.26	-3.08	-3.59	5.59
		Jul	-5.59	3.85	3.31	4.22	-3.01
		Oct	-7.44	-3.55	-2.61	2.47	2.72
		Jan	-5.11	-7.90	-10.62	-3.29	-0.03
	YSU	Apr	-9.65	-5.01	-6.63	0.47	-0.14
		Jul	-5.50	1.09	-1.33	2.48	-6.95
		Oct	-12.34	-1.44	-4.83	1.62	-7.79
	ACM2	Jan	-6.38	-9.54	-11.03	-4.56	-0.48
		Apr	-11.35	-5.91	-7.05	-0.86	-1.15
		Jul	-6.86	-0.64	-2.25	0.18	-7.96
		Oct	-14.11	-2.92	-5.69	-0.94	-8.85
	BL	Jan	-8.40	-10.47	-11.89	-5.01	-2.36
		Apr	-13.51	-8.00	-8.25	-2.07	-2.16
		Jul	-7.32	-1.75	-2.47	-0.23	-8.06
		Oct	-15.92	-3.51	-6.19	-0.91	-9.94
	MYJ	Jan	1.84	-3.86	-6.91	-0.69	6.86
		Apr	-3.89	-1.65	-3.44	1.91	5.84
		Jul	-1.68	3.02	0.42	3.61	-1.91
		Oct	-7.18	1.04	-2.50	3.36	-1.45
		Jan	1.33	1.92	1.58	2.17	0.59
	YSU	Apr	1.86	1.97	2.04	2.25	0.93
		Jul	1.35	1.56	1.20	1.79	1.30
		Oct	1.68	2.11	1.54	1.70	0.93
	ACM2	Jan	1.57	2.04	1.79	2.26	0.91
		Apr	2.11	2.01	2.18	2.37	1.21
		Jul	1.43	1.62	1.30	2.02	1.50
		Oct	1.90	2.19	1.73	2.05	1.21
	BL	Jan	1.50	2.02	1.63	2.40	1.01
		Apr	1.85	2.04	1.93	2.44	0.86
		Jul	1.21	1.54	1.12	1.72	1.10
		Oct	1.83	2.28	1.60	1.95	1.04
	MYJ	Jan	1.63	2.26	2.14	2.67	1.10
		Apr	2.33	2.40	2.65	2.69	1.61
		Jul	1.85	2.05	1.85	2.16	2.09
		Oct	2.01	2.58	2.17	2.12	1.55
		Jan	1.26	1.43	1.50	1.40	0.88
	YSU	Apr	1.51	1.49	1.67	1.22	1.07
		Jul	1.16	1.32	1.15	1.16	1.07
		Oct	1.42	1.45	1.40	1.14	1.04
	ACM2	Jan	1.88	1.91	1.97	2.21	1.36
		Apr	2.15	1.81	2.07	1.79	1.53
		Jul	1.56	1.62	1.50	1.71	1.59
		Oct	1.98	1.92	1.80	1.98	1.59



	Jan	2.32	2.32	2.13	2.74	1.63
	Apr	2.72	2.28	2.38	2.33	1.73
BL	Jul	1.79	2.09	1.75	2.08	1.71
	Oct	2.38	2.44	2.06	2.38	1.78
	Jan	1.63	1.76	1.94	2.18	1.45
	Apr	1.79	1.70	2.12	1.71	1.53
MYJ	Jul	1.42	1.56	1.52	1.42	1.66
	Oct	1.74	1.81	1.83	1.68	1.65

589

590 Similar to T_2 , 10-m wind speed (i.e., WS_{10}) is also a diagnostic variable of the near-surface wind
 591 speed. For the YSU, ACM2 and BL schemes, in the revised MM5 surface layer scheme, WS_{10} is
 592 calculated based on the Monin-Obukhov (M-O) similarity theory (Monin and Obukhov, 1954). The
 593 dimensionless profile function of momentum is denoted as:

594
$$\phi_m\left(\frac{z}{L}\right) = \frac{\kappa z}{u_*} \frac{\partial u}{\partial z} \quad (23)$$

595 where κ is the von Karman constant, u_* is the friction velocity, z is the height, L is the Obukhov
 596 length, integrating the Eq. (23) with respect to height z :

597
$$du = \frac{u_*}{\kappa} \left[\frac{dz}{z} - \frac{1 - \phi_m\left(\frac{z}{L}\right)}{L} d\left(\frac{z}{L}\right) \right] \quad (24)$$

598 integrate Eq. (24):

599
$$\int_0^u du = \frac{u_*}{\kappa} \left\{ \int_{z_0}^z \frac{dz}{z} - \int_{\frac{z_0}{L}}^{\frac{z}{L}} \left[1 - \phi_m\left(\frac{z}{L}\right) \right] d\ln\left(\frac{z}{L}\right) \right\} \quad (25)$$

600 here, let $\psi_m\left(\frac{z}{L}\right) = \int_0^{\frac{z}{L}} \left[1 - \phi_m\left(\frac{z}{L}\right) \right] d\ln\left(\frac{z}{L}\right)$, where $\psi_m\left(\frac{z}{L}\right)$ is the integrated similarity function
 601 for momentum.

602 Therefore, Eq. (25) can be indicated as $u = \frac{u_*}{\kappa} \left[\ln\left(\frac{z}{z_0}\right) - \psi_m\left(\frac{z}{L}\right) + \psi_m\left(\frac{z_0}{L}\right) \right]$, where z_0 is the
 603 roughness length.

604 Based on the bulk transfer method, the momentum flux can be represented as $\tau = \rho u_*^2 = \rho C_m u^2$,
 605 where τ is the momentum flux, C_m is the bulk transfer coefficient for momentum:

606
$$C_m = \frac{u_*^2}{u^2} = \frac{\kappa^2}{\left[\ln\left(\frac{z}{z_0}\right) - \psi_m\left(\frac{z}{L}\right) + \psi_m\left(\frac{z_0}{L}\right) \right]^2} \quad (26)$$

607 Thus, the wind speed at 10 m divided by the wind speed at a certain height can be written as:

608
$$u_{10} = \frac{u_*}{\kappa} \left[\ln\left(\frac{z}{z_0}\right) - \psi_m\left(\frac{z}{L}\right) + \psi_m\left(\frac{z_0}{L}\right) \right] \cdot \frac{\left[\ln\left(\frac{10}{z_0}\right) - \psi_m\left(\frac{10}{L}\right) + \psi_m\left(\frac{z_0}{L}\right) \right]}{\left[\ln\left(\frac{z}{z_0}\right) - \psi_m\left(\frac{z}{L}\right) + \psi_m\left(\frac{z_0}{L}\right) \right]} = \frac{u_*}{\kappa} \left[\ln\left(\frac{z}{z_0}\right) - \psi_m\left(\frac{z}{L}\right) + \right.$$

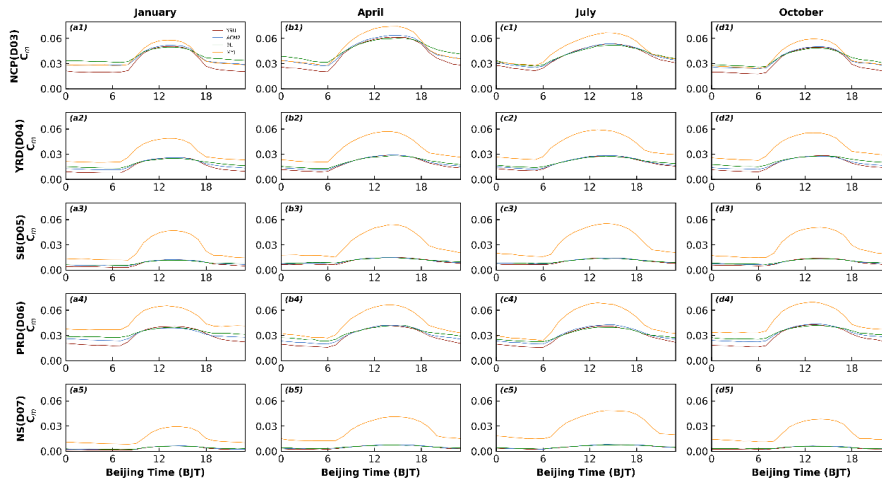
609
$$\left. \psi_m\left(\frac{z_0}{L}\right) \right] \cdot \left(\frac{C_m}{C_{m10}} \right)^{1/2} \quad (27)$$

610 where C_{m10} is the transfer coefficient for momentum at 10 m height:



$$611 \quad C_{m10} = \frac{\kappa^2}{\left[\ln\left(\frac{10}{z_0}\right) - \psi_m\left(\frac{10}{L}\right) + \psi_m\left(\frac{z_0}{L}\right) \right]^2} \quad (28)$$

612 Comparing the C_m of the three schemes (i.e., YSU, ACM2 and BL schemes) at night, C_m is the
 613 largest for the BL scheme, the second largest for the ACM2 scheme, and the smallest for the YSU
 614 scheme (Fig. 9). Correspondingly, the BL scheme simulates the largest WS₁₀, ACM2 the second
 615 largest, and the YSU the smallest (Fig. 8). The larger C_m corresponds to the stronger mixing, which
 616 transports more momentum from the upper to the lower layers, making WS₁₀ increase. Therefore,
 617 the bulk transfer coefficient C_m controls the variation of WS₁₀ at night. During the daytime, the C_m
 618 of the BL scheme is smaller than that of the other two schemes, and the corresponding WS₁₀ decrease
 619 (Fig. 8, 9). However, the difference among the three schemes is smaller in daytime than that in
 620 nighttime. The reason why the results of C_m and WS₁₀ differ with the same calculation method is
 621 because of the vertical variation of heat and momentum within the boundary layer involved in the
 622 calculation. This will correlate to the vertical diffusion coefficients within the boundary layer that
 623 will be discussed further in a later section.



624
 625 **Figure 9. Similar as Figure 2, but for momentum transfer coefficient (C_m).**

626 For the near surface scheme of the MYJ scheme, WS₁₀ is calculated according to the near surface
 627 flux profile relationship proposed by Liu et al. (1979):

$$628 \quad u_0 - u_s = D_1 \left[1 - \exp\left(-\frac{z_u u_*}{D_1 v}\right) \right] \left(\frac{F_u}{u_*} \right) \quad (29)$$

629 where 0 represents the value at height z above the surface where the molecular diffusivity still plays
 630 a dominant role, s denotes the surface value, D_1 denotes a near surface parameter, u_* is the friction
 631 velocity, v is the molecular diffusivity for momentum ($=1 \times 10^{-5}$), and F_u is the momentum flux.

$$632 \quad \text{Since } 1 - \exp\left(-\frac{z_u u_*}{D_1 v}\right) \approx \frac{z_u u_*}{D_1 v}, \quad u_0 - u_s = \left(\frac{z_u}{v}\right) F_u.$$



633 The momentum flux in the surface layer above the viscous sublayer is represented by $F_u =$
 634 $\left(\frac{C_m}{\Delta z_e}\right)(u_{low} - u_0)$, here, the subscript *low* denotes the variables at the lowest model level, Δz_e is
 635 either the equivalent height of the lowest model level that considers the presence of the “dynamical
 636 turbulence layer” at the bottom of the surface layer (Janjić, 1990). C_m is the bulk transfer coefficient,
 637 defined as:

$$638 \quad C_m = \frac{\kappa u_*}{\ln\left(\frac{z_0+z}{z_0}\right) + \psi_m\left(\frac{z_0+z}{L}\right) - \psi_m\left(\frac{z_0}{L}\right)} \quad (30)$$

639 In Eq. (29), z_u is still an unknown, such that $\frac{z_u u_*}{D_1 v} = \xi$, where ξ is a smaller constant (equal to
 640 0.35 in the model). Here, the near surface parameter D_1 is further defined as $D_1 = C \cdot$
 641 $\left(\frac{z_0 u_*}{v}\right)^{1/4}$, where C is a constant (=30), the roughness length z_0 as a function of u_* ($z_0 = \frac{0.11v}{u_*} +$
 642 $\frac{0.018u_*^2}{g}$), substituting D_1 and z_u to Eq. (29):

$$643 \quad u_0 = \frac{\frac{\xi}{u_*} \left[C \left(\frac{z_0 u_*}{v} \right)^{1/4} \right] \left(\frac{C_m}{\Delta z_e} \right) u_{low} + u_s}{1 + \frac{\xi}{u_*} \left[C \left(\frac{z_0 u_*}{v} \right)^{1/4} \right] \left(\frac{C_m}{\Delta z_e} \right)} \quad (31)$$

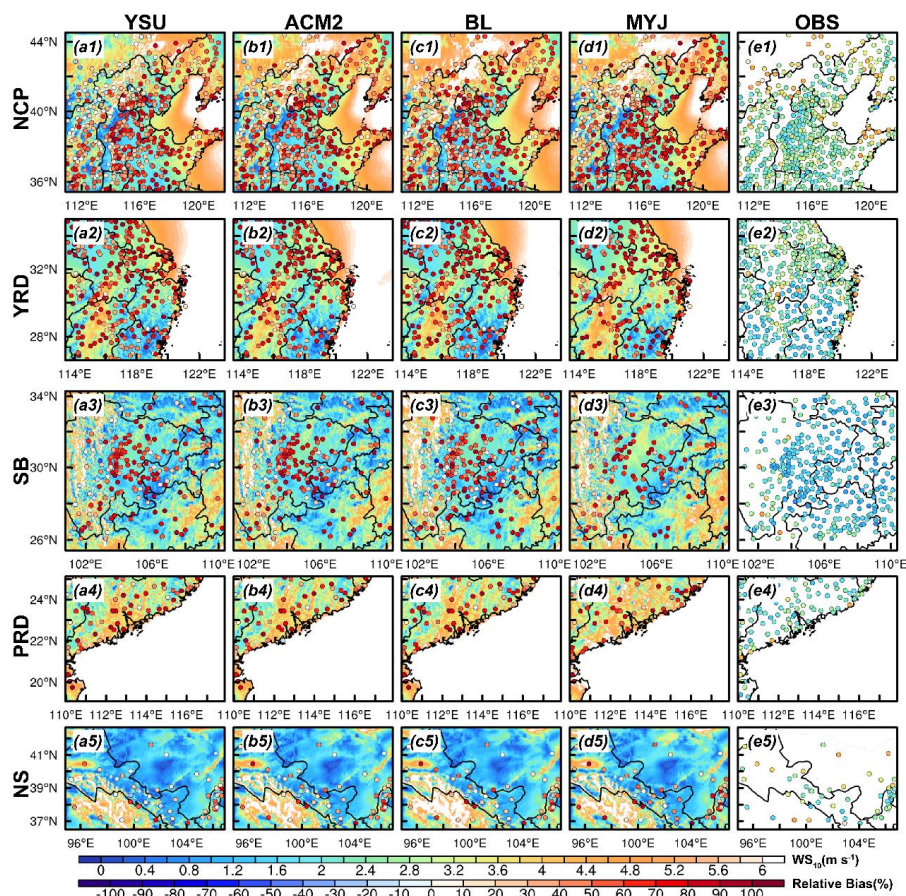
644 The wind speed at a height of 10 m can be expressed as:

$$645 \quad u_{10} = \frac{F_u \Delta z_e}{C_{m10}} + u_0 = \frac{C_m (u_{low} - u_0)}{C_{m10}} + u_0 \quad (32)$$

646 where C_{m10} is the transfer coefficient for momentum at 10 m height:

$$647 \quad C_{m10} = \frac{\kappa u_*}{\ln\left(\frac{z_0+10}{z_0}\right) + \psi_m\left(\frac{z_0+10}{L}\right) - \psi_m\left(\frac{z_0}{L}\right)} \quad (33)$$

648 Therefore, the C_m of the MYJ scheme is significantly different from the other three schemes. Except
 649 for the NCP region, although the C_m of the MYJ scheme is larger than the other three schemes at all
 650 times of the day, the WS_{10} presents the maximum only during the daytime. This suggests that at
 651 night, the wind speed simulated by the MYJ scheme also be influenced by other factors. For example,
 652 the calculation method of the integrated similarity functions (ψ_m) in the MYJ scheme is different
 653 from the other three schemes. In the other three schemes, the ψ_m is calculated according to four
 654 stability regimes defined in terms of the bulk Richardson number (Zhang and Anthes, 1982). In the
 655 MYJ scheme, the ψ_m is calculated based on two stability regimes by the z/L (Paulson, 1970).



656

657 **Figure 10. Similar as Figure 5, but for 10-m wind speed.**

658

659

660

661

662

663

664

665

666

667

668

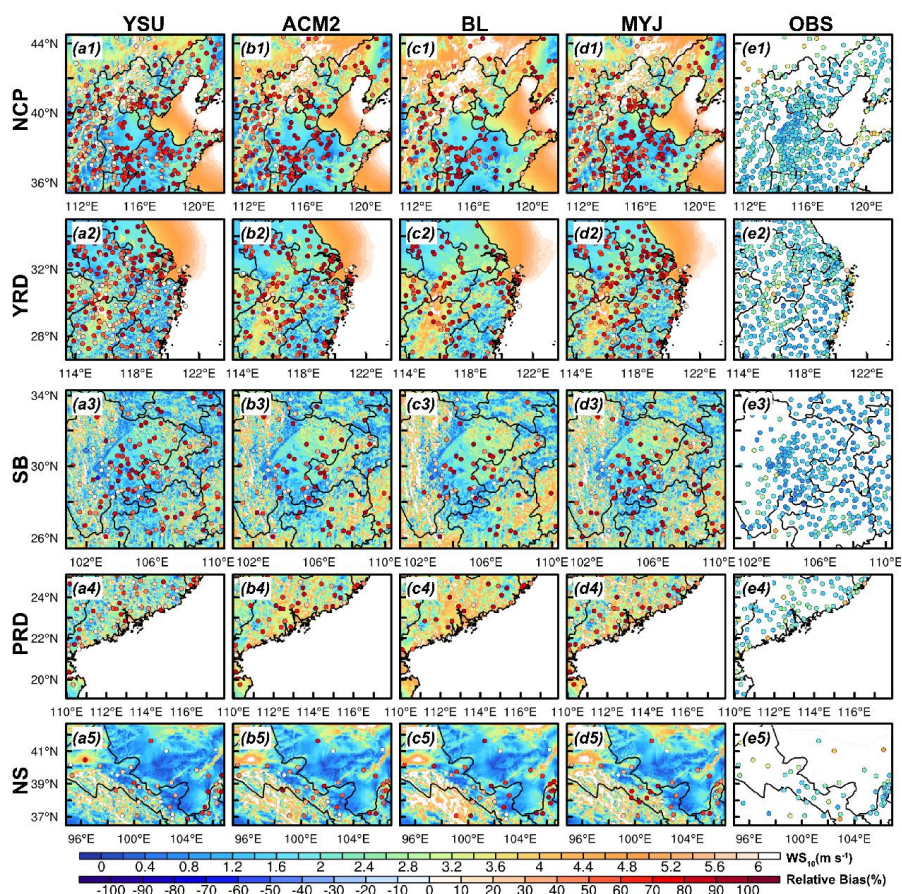
669

670

The reasons for the differences in WS_{10} simulation are further analyzed in terms of regional distribution. During the daytime, wind speed is significantly overestimated at most sites throughout the NCP region, which are centered in the plains and valleys, but is less overestimated and even underestimated at some sites on the mountain tops (Fig. 10, S13-S15 a1-e1). Wind speed is overestimated at almost all stations throughout the YRD and PRD regions (Fig. 10, S13-S15 a2-e2, a4-e4). The WS_{10} in the basin is importantly overestimated in the SB region, while less overestimated at hilltop stations on the eastern side of the basin, with higher wind speed being more pronounced in January (Fig. 10, S13-S15 a3-e3). In the NS region, wind speed is overestimated to a lesser extent than in other regions, but for regions with lower wind speed, the relative bias (RB) is larger, especially in July (Jan: RB=29.3%~49.1%, Apr: RB=32.0%~55.6%, Jul: RB=44.2%~78.7%, Oct: RB=42.7%~65.7%). Comparing the simulation results of the four schemes, the MYJ scheme simulates the most significantly overestimated wind speed and the least overestimated for the YSU scheme (Fig. 10, S13-S15). In comparison with the four months, it is



671 found that the RB of the simulation is the largest for the month with slower wind speed (i.e., July).
672 At night, the wind speed is overestimated at almost all stations in the whole region of NCP, and the
673 overestimation is greater at the hilltop stations than during the day (Fig. 11, S16-S18). The other
674 four regions are more similar to the daytime (Fig. 11, S16-S18). However, by comparing the four
675 schemes, we find that the BL scheme has the most obvious overestimation, different from the
676 daytime, while the YSU scheme still has the lowest overestimation, the same as the daytime. In
677 general, wind speed is smaller at night, and the four schemes overestimate wind speed much more
678 than during the day. Averaging the RB of wind speed over the five regions and four months, the
679 daytime (nighttime) values for the YSU, ACM2, BL and MYJ schemes are 77.7% (92.4%), 85.6%
680 (123.6%), 80.2% (146.0%), and 100.8% (117.4%), respectively. This simulated misestimation of
681 low winds at night may mainly originate from the inapplicability of the M-O similarity theory. The
682 strong stable boundary layer usually occurs on nights with low winds (Monahan and Abraham, 2019;
683 Vignon et al., 2017). In this strong stable boundary layer, turbulence occurs weakly and
684 intermittently, the turbulence intensity is disproportionate to the mean gradient, and the M-O
685 similarity theory is no longer applicable (Acevedo et al., 2015; Sun et al., 2012). Ultimately, these
686 inapplicable functions affect the calculation of the bulk transfer coefficient and can further lead to
687 large deviations in the simulation of wind speed.



688

689 **Figure 11. Similar as Figure 6, but for 10-m wind speed.**

690

691

692

693

694

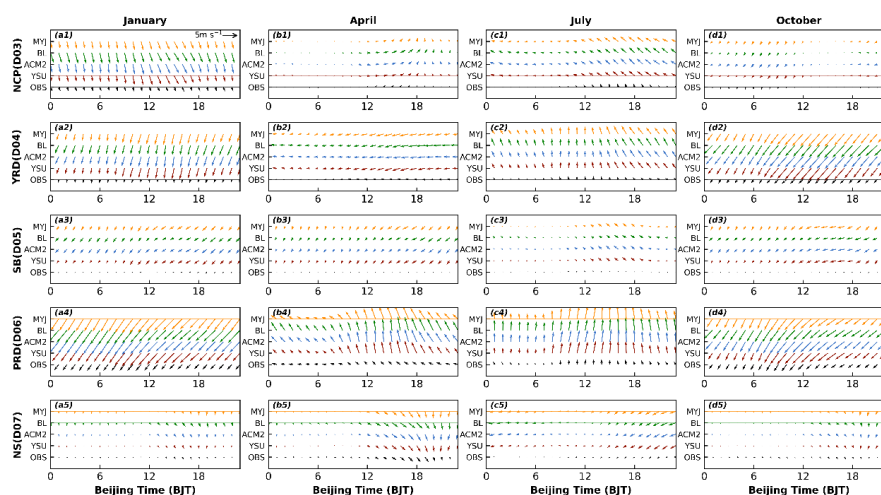
695

696

697

698

We further re-analyze the effect of topography on wind speed. The wind speed is overestimated for plains and valleys and better reproduced/underestimated for mountain tops, mainly because of the smoother topography in the model. This is rather because coastal stations in the plains, many of which also have high wind speeds, are not well reproduced and still show significant overestimation (Fig. 10), than the high wind speeds at the top of the mountains, which are better simulated. It is assumed that the wind speed should be small in plain areas with complex underlying surface, but it increases after the model has smoothed the terrain. The wind speed increases gradually with height, and when the terrain at the top of the mountain is smoothed, the originally larger wind speed decreases, and the wind speed will be closer to the observed value.



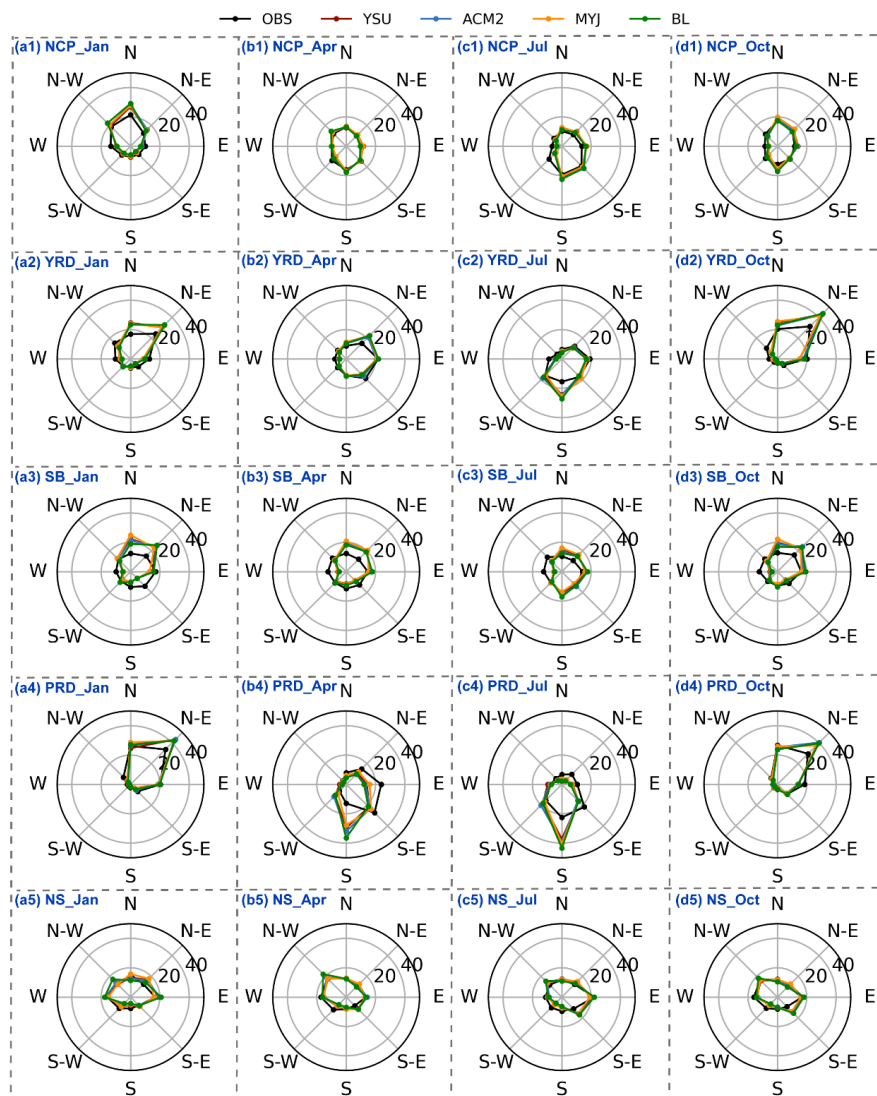
699

700 **Figure 12. Similar as Figure 2, but for 10-m wind direction.**

701 The model can basically simulate the changes of wind direction in the five regions, well capturing
702 the overall wind direction in each region (Fig. 12). In the NCP region, the simulation of wind
703 direction is poor in January compared to the other three months, with a high frequency of
704 northwesterly-northerly winds, overestimated by about 6.6% (Fig. 13 a1-d1). In addition, coupled
705 with larger wind speed, it causes the effect of advective transport to be amplified, thus affecting the
706 variation of pollutant concentrations (W. Jia and Zhang, 2021). The frequency of simulated
707 northeasterly winds in the YRD region is higher than that observed in January (~6.9%), April
708 (~6.9%) and October (~11.2%), while the frequency of southerly winds is higher in July (~10.0%)
709 (Fig. 13 a2-d2). The wind direction of SB region is poorly simulated since the topography is too
710 complicated in the SB region, with a basin in the middle and high topographic mountains all around
711 (Fig. 13 a3-d3). The low wind state in the middle of the basin is difficult to be captured. The
712 percentage of northeasterly winds simulated by the model in January, April, July and October are
713 22.9%~25.6%, 19.2%~20.6%, 14.9%~16.4%, 22.4%~24.2%, respectively, and the percentage of
714 observations are 15.1%, 12.0%, 10.9%, 16.1%, respectively. Similarly, the percentage of westerly
715 winds simulated by the model in January, April, July and October are 4.7%~5.1%, 4.7%~5.7%,
716 4.8%~5.5%, 3.8%~5.1%, respectively, and the percentages of observations are 9.9%, 12.4%, 12.4%,
717 12.3%, respectively. The model simulates a large proportion of northeasterly winds and a smaller
718 proportion of westerly winds (Fig. 13 a3-d3). In the PRD region, the frequency of northeasterly
719 wind occurrences in January and October is significantly overestimated by about 8.8% and 9.5%,
720 while the frequency of southerly winds is overestimated in April and July by about 14.5% and 17.3%,
721 and the frequency of southeasterly winds is underestimated (Fig. 13 a4-d4). The wind direction is
722 better simulated in the NS region, not significantly influenced by the complex terrain (Fig. 13 a5-



723 d5).



724
 725 Figure 13. Wind-rose plots in five regions for four seasons are (a1-d1) NCP region, (a2-d2) YRD
 726 region, (a3-d3) SB region, (a4-d4) PRD region and (a5-d5) NS region, respectively.
 727

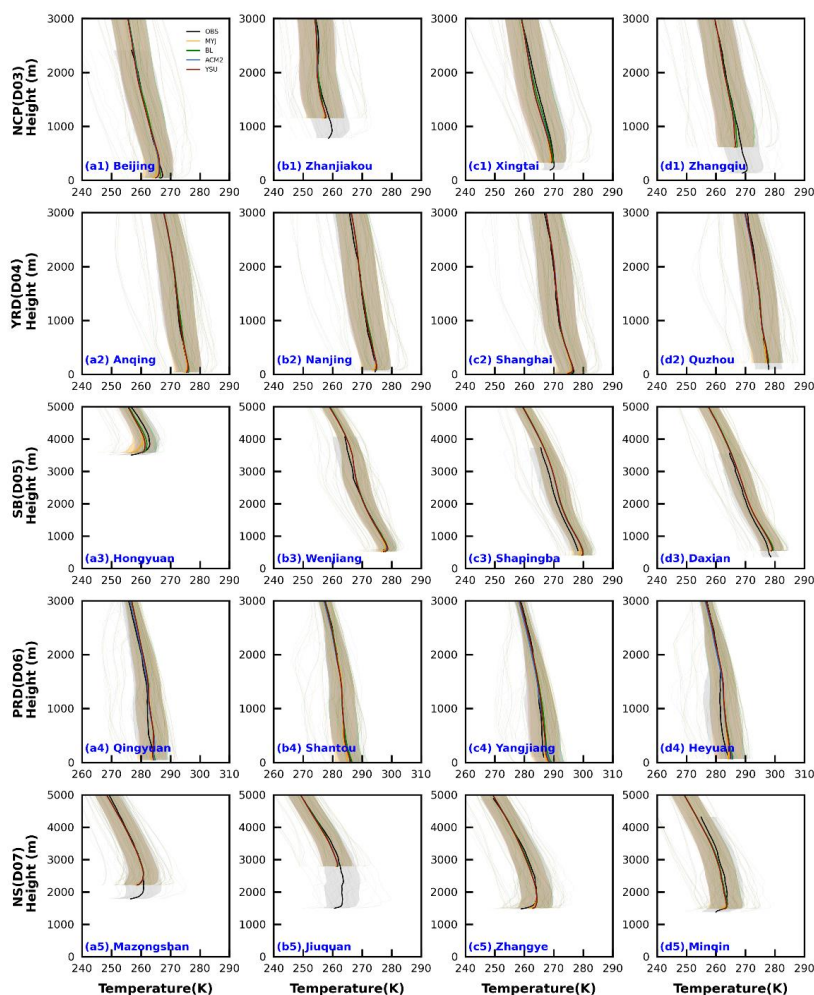
728 3.2 Vertical structures

729 To better understand the performance of model in simulating PBL structure under different
 730 underlying surface, four representative stations have been selected in each region, with stations in
 731 plain areas, stations in mountains areas with high elevation, and stations near the sea.



732 3.2.1 temperature

733 Accurate simulation of the vertical structure of the PBL is very important for the evolution of
734 pollution, precipitation and typhoons. In the vertical direction, four typical sounding stations are
735 selected for each region at 08:00 to better reflect the simulation of the vertical structure of the PBL
736 under different underlying surface conditions. Overall, the model captures the vertical structures of
737 the temperature. From the simulation results in January, the best reproduction of the temperature
738 simulation is found in the YRD region, in which the temperature is closer to the observed values
739 (Fig. 14 a2-d2). In addition to the NCP, SB and NS regions, a temperature inversion layer appears
740 in the lower layers at 08:00, and the NS region has the most significant temperature inversion (Fig.
741 14 a1-d1, a3-d3, a5-d5). The model does not simulate the temperature variation of the inversion
742 layer well, and shows significant differences from the observations. When there is a difference in
743 topography between the observed and simulated stations, the bias in the temperature is more
744 pronounced. These stations usually exist in complex topographic conditions, such as Zhangjiakou
745 and Zhangqiu stations in the NCP region, Shapingba in the SB region, and Mazongshan and Jiuquan
746 in the NS region (Fig. 14 b1, d1, c3, a5, b5). The topographic discrepancy caused by the lack of
747 high resolution may, on the one hand, account for it, resulting in more complex topography in the
748 grid points closest to the observation stations. On the other hand, there is also an urgent need for
749 finer underlying surface data to respond more closely to the observed real topography. The effect of
750 resolution and underlying surface will be discussed in detail in the **Part II**. Although the elevation
751 of the Hongyuan station in the SB region is higher, the difference in topographic height obtained
752 from observations and simulations are close to each other (Fig. 14 a3).



753

754

755

756

757

758

759

760

761

762

763

764

Figure 14. Average vertical profiles of observed and simulated temperature at 08:00 and 20:00 BJT at four sounding stations for each region in January (Winter). The unobtrusive gray lines indicate the simulated lines for all time periods, and the lines with shading indicate the average values and shaded areas show the uncertainty range (the mean ± 1 standard deviation).

There is an underestimation of temperature at stations with higher topography and overestimation for lower topography, which is more consistent with the conclusions drawn from 2-m temperature (Fig. 5, 14). However, the underestimation of temperature is not present throughout the vertical, but is more pronounced in the lower layers, which are more influenced by the underlying surface. From the differences of the four schemes, the MYJ scheme simulates the lowest temperature and largest temperature gradient. Since the MYJ scheme simulates a weak turbulent diffusion of heat, a well vertical exchange process cannot occur, bringing into a large temperature gradient (Fig. S19). The



765 differences of the four schemes gradually decrease with the increase of the height. The BL scheme,
766 which is also a local closure scheme, with a smaller vertical gradient in temperature, mainly because
767 this scheme adds a counter-gradient correction term to the heat flux, which is mainly applicable to
768 the convective PBL(Bougeault and Lacarrere, 1989). The presence of this term leads to an increase
769 in turbulent diffusion and a decrease in temperature gradient. However, it is worth noting that there
770 are still slightly stable stratifications at 08:00, and this term generates upward heat flux and reduces
771 the temperature gradient, which is closer to the results of the nonlocal closure schemes (YSU and
772 ACM2 schemes). The simulation results for the other three months are not as good as January, but
773 the simulation characteristics are similar to January (Figures not shown). The results at 20:00 are
774 similar to those at 08:00, and thus will not be repeated here (Figures not shown).

775 3.2.2 wind speed and direction

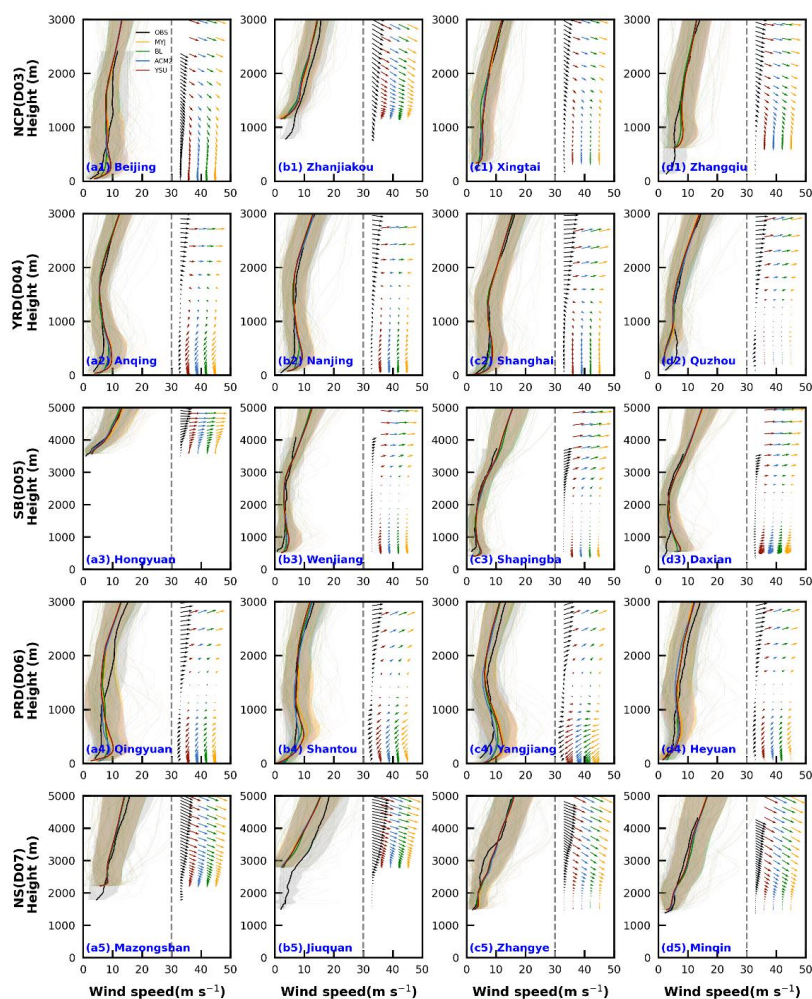
776 The simulation of wind speed vertical structure is much worse in comparison to temperature (Fig.
777 14, 15). The simulated results of wind speed in the vertical direction and 10-m wind speed are still
778 quite different. In the four months, the wind speed is almost overestimated at the lower altitude
779 stations below 1000 m in all the four regions except the NS region, and wind speed is less
780 overestimated in July than in the other three months (Fig. 15, S20-S22 a1-d4). However, for the NS
781 region, the wind speed is almost better simulated, or underestimated, and is significantly different
782 from the other four regions (Fig. 15, S20-S22 a5-d6). We can compare the Zhangjiakou station in
783 the NCP region with the Hongyuan station in the SB region, and find that the wind speeds at these
784 stations are almost not overestimated (Fig. 15 b1, a3). The effect of the model on terrain smoothing
785 contributes to it. Because the wind speed itself increases with the increase of height, and it decreases
786 when the model smooths over the terrain.

787 Unlike the 10-m wind speed, the simulation results of the 10-m wind speed have the smallest bias
788 for the YSU scheme, which is closer to the observed value (Table 2, Figs. 8, 10-11). Of course, this
789 phenomenon can also be found from the evolution of the wind speed in the vertical direction (Fig.
790 15, S20-S22). However, as the height increases, the bias of the YSU scheme gradually increases and
791 is greater than the other three schemes (Fig. 15, S20-S22). Such a large vertical gradient of wind
792 speed in the YSU scheme indicates a weak mixing in this scheme. From the turbulent diffusion
793 coefficients of the momentum at 08:00 in January, it is true that the YSU scheme simulates the
794 smallest turbulent diffusion coefficient below 1000 m (Fig. S23). While the BL scheme simulates a
795 smallest vertical gradient of wind speed, which corresponds to the largest turbulent diffusion
796 coefficient of momentum (Fig. S23). The time variation characteristics of the turbulent diffusion
797 coefficient will be deliberated and analyzed in detail later.

798 The simulation results of wind direction notes that the model can capture the characteristics of wind
799 direction well, and it also simulates well for the stations with more complicated topography and



800 higher altitude (Figs. 15, S20-S22).



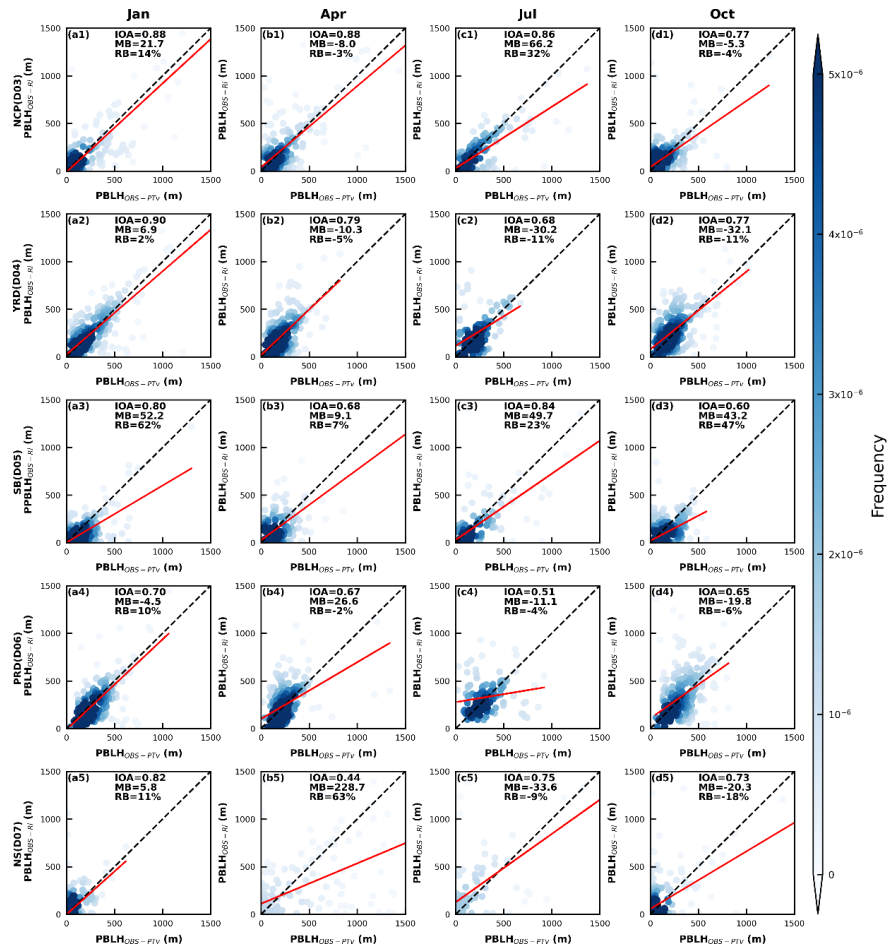
801
 802 **Figure 15.** Similar as Figure 14, but for 10-m wind speed and direction.
 803

804 3.3 PBLH

805 Based on the observed data, comparing the PBLH calculated by the two methods, it is found that
 806 the results are mixed for two methods (Fig. 16). The results for January (IOA=0.70~0.90) are better
 807 than the other three months (IOA=0.44~0.88 in April, IOA=0.51~0.86 in July, IOA=0.60~0.77 in
 808 October), and the results in the NCP region are better than the other four regions (Fig. 16). The
 809 PBLH in the NS region are more scattered, unlike the other regions where most of the PBLH are
 810 concentrated below 500 m, especially in April and July (Fig. 16 b5-c5). On the whole, the difference



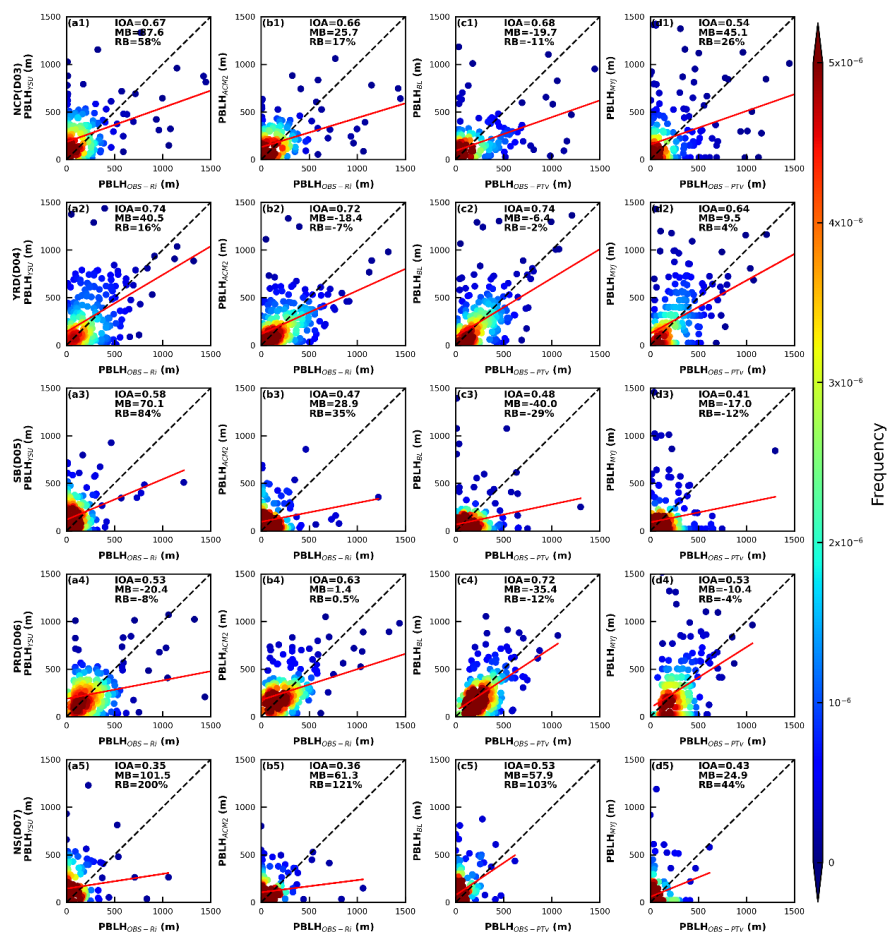
811 in PBLH calculated by the two methods is more obvious in the NS region with more complex
 812 topography, which is especially noted when calculating in this type of underlying surface region.



813
 814 **Figure 16. Density scatterplots of the PBLH by the two methods in five regions for four seasons.**
 815 Further, the mechanism of understanding the PBLH differences based on different stations from
 816 different regions. The planetary boundary layer height (PBLH) for the YSU and ACM2 schemes is
 817 calculated by the Richardson number method, and the PBLH for the BL scheme is obtained by the
 818 virtual potential temperature method (see Section 2 for details). The same two methods are also used
 819 to calculate the PBLH with sounding data for comparison (Eqs. 29 and 30). First, we compare the
 820 PBLH calculated based on the observed data using Richardson number (Ri) with the PBLH
 821 simulated by YSU and ACM2 schemes. The Ri is determined by both buoyancy term and the shear
 822 term together (Eq. 29). The difference between simulated and observed temperature gradient is
 823 smaller than the wind speed gradient within the PBL (Figs. 14-15). Therefore, the difference in Ri



824 mainly comes from the variation in the shear term. The wind speed gradient simulated in both
825 schemes are greater than the observed values (Fig. 15), except for individual stations, which would
826 result in small values of Ri . Thus, the height of Ri up to 0.25 would be high and the PBLH would
827 be high. Consequently, the PBLH simulated by the YSU and ACM2 schemes are higher than the
828 observed values at most stations. For example, in the case of the Quzhou station in the YRD region,
829 the simulated wind speed gradient at this station is much smaller than the observed value in January,
830 thus, the simulated PBLH is correspondingly smaller than PBLH calculated from observations (Figs.
831 15, S24 d2). Comparing the results of the other three months, we can also find similar conclusions
832 (Figures not shown). The wind speed gradient simulated by the YSU scheme is larger than that of
833 the ACM2 scheme, and therefore the PBLH is larger than that of the ACM2 scheme, except for the
834 Shanghai station in the YRD region, Shantou and Yangjiang stations in the PRD region (Fig. S24).
835 For the ocean, the PBLH simulated by the ACM2 scheme is higher than that of the YSU scheme,
836 while for most areas adjacent to the ocean, the PBLH simulated by the ACM2 scheme is on the high
837 side in the YRD and PRD regions (Fig. S25). The simulated PBLH of the BL scheme is in better
838 agreement with the PBLH calculated by the virtual potential temperature method, which is
839 substantially better than the other three schemes. The PBLH simulated by the MYJ scheme is mixed
840 (Fig. 17).



841
 842 **Figure 17. Density scatterplots of observed and simulated PBLH by four PBL schemes in five**
 843 **regions in January (Winter).**
 844 From the differences of regional distributions, the region with the best PBLH simulation result is
 845 the YRD region in January, (IOA=0.64~0.74; MB=-6.4~40.5 m; RB=-2%~16%), followed by the
 846 PRD region (IOA=0.53~0.72; MB=-35.4~1.4m; RB=-12%~0.5%), and the worst simulation results
 847 for the PBLH in the NS region (IOA=0.35~0.53; MB=24.9~101.5 m; RB=44%~200%) (Fig. 17).
 848 Also, the PBLH simulation in the SB region is poorer and slightly better than that in the NS region,
 849 noting that there is still much potential for the model to improve the reproduction of the PBLH in
 850 complex terrain. From the simulation results of the four schemes, the PBLH simulated by the BL
 851 scheme is the closest to the observed value, followed by the YSU and ACM2 schemes, and the
 852 PBLH simulated by the MYJ scheme is the worst in that the simulation results of temperature are
 853 better compared with other meteorological factors, so the method of judging the PBLH using the
 854 virtual potential temperature will be more consistent with the observed values. While as the YSU



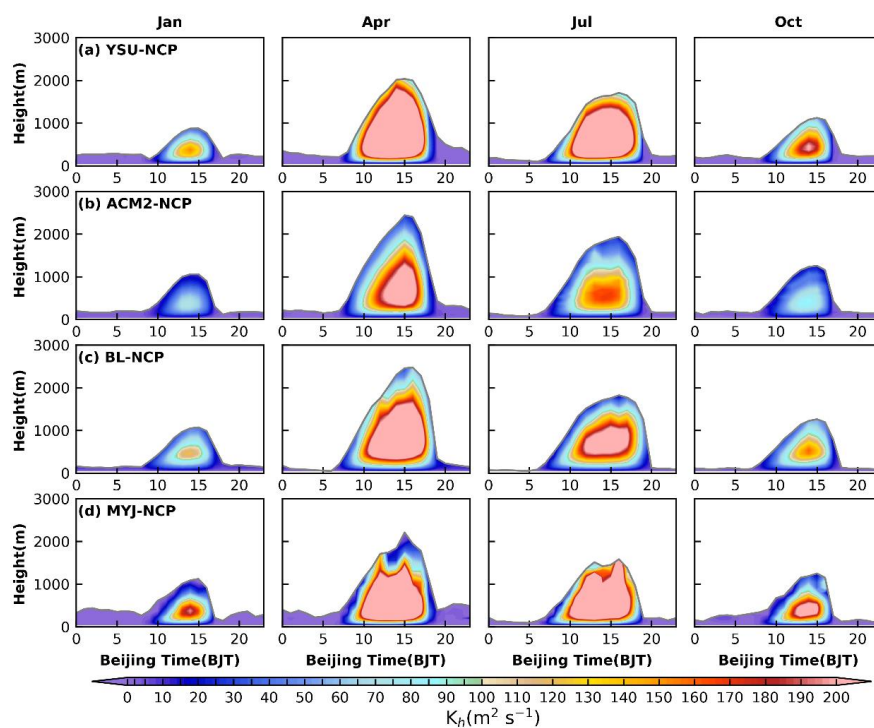
855 and ACM2 schemes using Richardson number method will involve the wind speed gradient, and
856 the vertical gradient of wind speed is poorly simulated below 1000 m. That's why it will affect the
857 judgment of the PBLH. If the simulation results of vertical gradient of wind speed can be improved
858 subsequently, then the simulation results of PBLH of these two schemes will be improved to some
859 extent. There are not enough observations to calculate the PBLH using TKE, so there will be some
860 differences with the PBLH simulated by the MYJ scheme. The mean bias of the simulation increased
861 in April and July when the PBLH is higher compared to January, with mean bias of -29.6~361.8 m
862 (6.5~603.9 m), -12.6~410.6 m (41.6~603.2 m), -34.1~301.1 m (3.2~683.9 m) and -14.5~96.3 m (-
863 11.3~523.6 m) for the YSU, ACM2, BL and MYJ schemes in April (July), respectively. Similar to
864 January, the best simulation results have been obtained for the YRD (MB=7.8~72.4 m in April,
865 MB=28.5~66.5 m in July) and PRD (MB=-34.1~-12.6 m in April, MB=-11.3~54.8 m in July)
866 regions, and the worst for the NS region (MB=61.8~410.6 m in April, MB=523.6~683.9 m in July).
867 The results for October are more similar to those for January, with lower PBLH and better
868 simulations than those for April and July (Figures not shown).

869 3.4 turbulent diffusion coefficient

870 Since the model itself does not directly output turbulent diffusion coefficients for all schemes, there
871 is relatively little direct comparison and analysis of this parameter. As seen in section 3.3.2 above,
872 the turbulent diffusion coefficient (TDC) plays a crucial role in the momentum vertical transport
873 within the PBL and also has an impact on the diffusion of other parameters, such as heat, water
874 vapor and pollutants (Ding et al., 2021; R. B. Stull, 1988). The accurate portrayal of the TDC directly
875 affects the evolution of the PBL structure. Based on the contents of section 2.3, the momentum TDC
876 is not equal to the heat TDC under unstable and neutral conditions for the YSU scheme, and the
877 momentum TDC is equal to the heat TDC under stable conditions. The ACM2 scheme uses the
878 MOST method to calculate the TDC as the YSU scheme, but also considers the TDC calculated by
879 the mixing length theory. The momentum TDC is not equal to the heat TDC in the MYJ scheme,
880 while the momentum TDC is equal to the heat TDC in the BL scheme. Because of the difference in
881 altitude of different stations, Beijing station in the NCP region, Nanjing station in the YRD region,
882 Daxian station in the SB region, Qingyuan station in the PRD region and Zhangye station in the NS
883 region were selected as representative stations to analyze the turbulent diffusion characteristics.
884 Here, the TDC of heat is taken as an example, the following basic characteristics have been found.
885 (1) the YSU and MYJ schemes have the largest TDC during the day, followed by the BL scheme,
886 and the ACM2 scheme has the smallest TDC (Fig. 18). (2) The TDC is largest in April and July, and
887 smallest in January and October (Fig. 18). (3) There are significant seasonal differences in the PBLH
888 for the NCP, SB and NS regions, while for the YRD and PRD regions. The difference in the PBLH
889 affects the variation of the turbulent diffusion, especially for the YSU and ACM2 schemes, where



890 the PBLH is used during the calculation of the turbulent diffusion. In the YSU scheme, the TDC of
891 momentum is calculated first, and then the TDC of heat is calculated with the Prandtl number (Pr).
892 Thus, the variation of the PBLH is proportional to the TDC (Fig. 18a). While in the ACM2 scheme,
893 the TDC of heat is calculated directly based on the dimensionless function of heat. Moreover, the
894 Pr in the YSU scheme varies with height, while the Pr in the ACM2 scheme is a constant (=0.8). It
895 is also worth noting that in the ACM2 scheme, another TDC is calculated using the mixing length
896 theory, and the change of the empirical stability function in the mixing length method changes the
897 TDC. Therefore, the YSU scheme calculates a large TDC of momentum, which also leads to a large
898 TDC of heat. The TDC of heat in the ACM2 scheme, on the other hand, will be affected by the
899 mixing length method, and differs from the calculation principle of the YSU scheme.



900
901 **Figure 18. Time-height cross sections of heat turbulent diffusion coefficient simulated by (a) YSU**
902 **scheme, (b) ACM2 scheme, (c) BL scheme and (d) MYJ scheme for four seasons in the NCP region.**
903 **The gray line indicates the PBLH.**

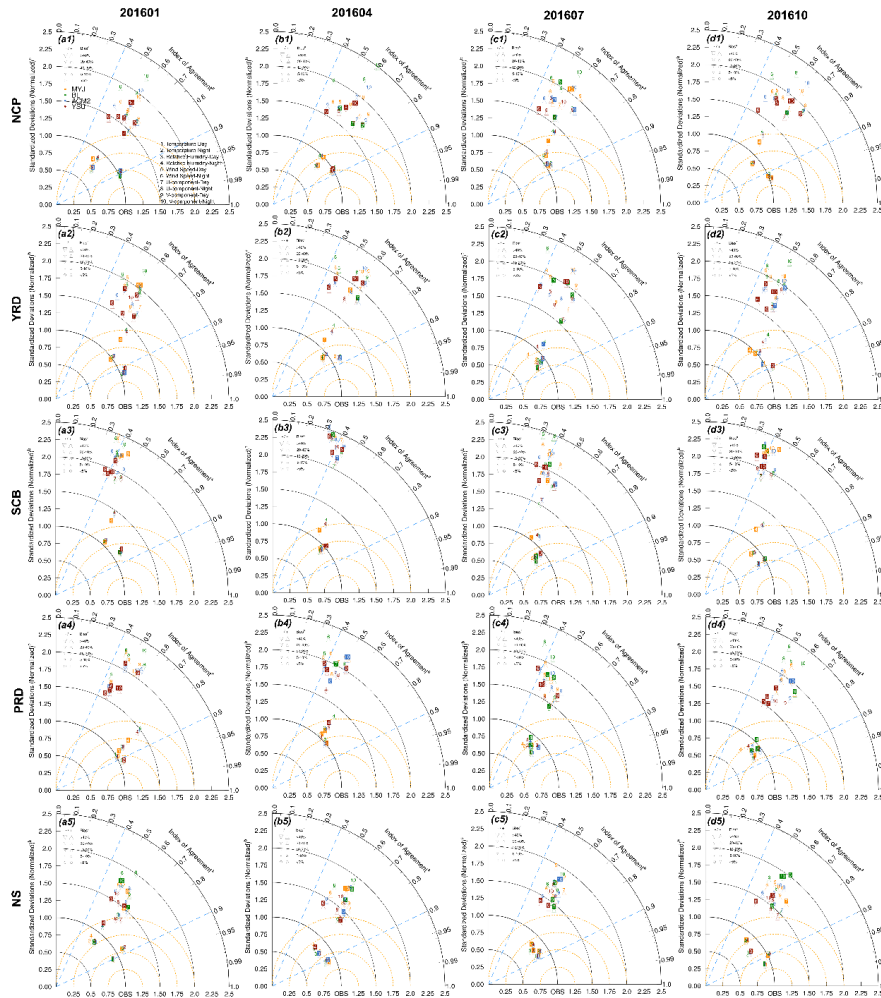
904 From the section 3.2.2 above, it is clear that the BL scheme has the strongest turbulent diffusion at
905 08:00, making the vertical gradient smaller, especially the wind speed is large. Similarly, this
906 phenomenon can be found in the daily variation of turbulent diffusion, and not only at 08:00, but
907 almost throughout the night (Fig. 18). The difference between MYJ and BL schemes is mainly
908 reflected in the calculation principle of mixing length, which is not directly related to the PBLH. In



909 the BL scheme, mixing length scale can be relative to the distance that a parcel originating from this
910 layer, can travel upward and downward before being stopped by buoyancy effects (Eq. 14).
911 Therefore, the vertical height below the temperature inversion layer at night, with the surface as the
912 lower boundary, is the length scale of turbulence, i.e., mixing length scale. While in the MYJ scheme,
913 the mixing length scale is equal to z minus the integral depth scale, which is equal to the height of
914 the equal-area rectangle under the profile. It is worth noting that the mixing length scale in the BL
915 scheme mainly considers the effect of thermal and takes temperature gradient as the criterion, while
916 the turbulent length scale in the MYJ scheme is mainly determined based on the TKE. TKE is further
917 divided into horizontal TKE and vertical TKE. Horizontal TKE is mainly influenced by wind shear
918 and the turbulent eddy scale can reach 1.5~3 times the PBLH on the horizontal, and even reach 6
919 times the PBLH (Atkinson and Zhang, 1996). The vertical depth of an unstable layer capped by an
920 inversion is automatically selected as the length scale for turbulence in the BL scheme during the
921 daytime. Moreover, in the BL scheme, there is a counter-gradient correction term in the convective
922 PBL, which leads to a downward transport of dry and cool air, making the thermal reach a lower
923 height and a smaller length scale for turbulence. We also find that the PBLH of the MYJ scheme
924 exhibits a “sawtooth”, and is more pronounced at night. This is mainly because the turbulence is
925 weaker at night, and presents intermittent characteristics, which, together with the judgment method
926 of PBLH and the coarse vertical resolution, can cause such variation of the PBLH. Although the
927 improvement of PBLH in the MYJ scheme cannot have a substantial effect on turbulent diffusion,
928 the threshold value of its determination method is open to question.

929 3.5 Discussion of optimal PBL schemes

930 To better understand the simulation performance of different PBL parameterization schemes for
931 different parameters in each region, this section will discuss the expressiveness of different PBL
932 schemes through the statistical approach. Figure 19 shows the Taylor statistics for the analysis of
933 near-surface meteorological parameters in four months in five regions.



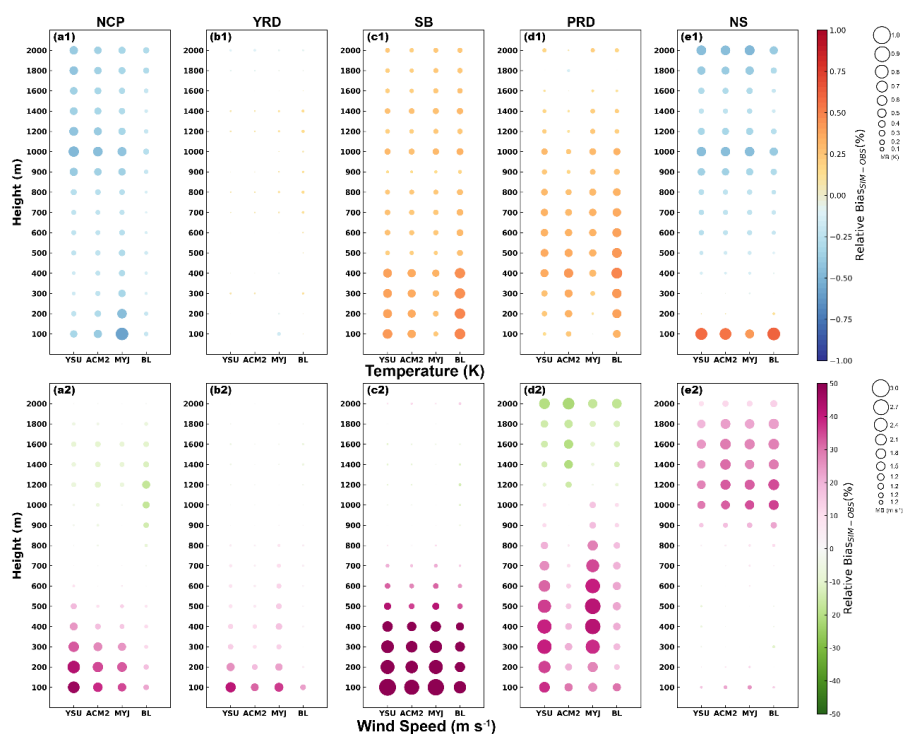
934
 935 **Figure 19. Taylor diagram of observation and simulation in five regions for four seasons. XY axes**
 936 **and arc represent the normalized standardized deviations (NSDs; NSD =**
 937
$$\frac{\sqrt{\frac{1}{N-1} \sum_{i=1}^n (X_{sim,t} - \bar{X}_{sim})^2}}{\sqrt{\frac{1}{N-1} \sum_{i=1}^n (X_{obs,t} - \bar{X}_{obs})^2}}, \bar{X}_{sim}$$
 and \bar{X}_{obs} **represent the average value of simulation and observation,**
 938 **respectively) and index of agreement (IOA; IOA =**
$$1 - \frac{[\sum_{i=1}^n |X_{sim,t} - X_{obs,t}|^2]}{[\sum_{i=1}^n (|X_{sim,t} - \bar{X}_{obs}| + |X_{obs,t} - \bar{X}_{obs}|)^2]}$$
 , $X_{sim,t}$ and
 939 **$X_{obs,t}$ represent the value of simulated and observed, respectively; i refers to time, and n is the**
 940 **total number of time series), respectively. Four schemes are shown in different colors, and different**
 941 **numbers represent different parameters. The root mean square is denoted by orange dashed line**
 942 **and the relative bias (RB; RB =**
$$\frac{\bar{X}_{sim} - \bar{X}_{obs}}{\bar{X}_{obs}} \times 100\%$$
) is shown by different symbols.



943 For the NCP region, the 2-m temperatures are underestimated during the daytime in January (Fig.
944 2), while the BL scheme simulates the highest temperature, so the BL scheme performs optimally.
945 Although the temperatures are somewhat overestimated at night, the overestimated period is shorter.
946 The IOA of the four schemes is similar, with the ACM2 scheme having a slightly smaller bias (Fig.
947 19 a1). Combined with the regional distribution of all stations in the NCP region, the BL scheme is
948 recommended if the study area is mainly for Beijing, while the ACM2 and YSU schemes are
949 recommended for the south of the NCP in January, such as Shandong Peninsula and southern Hebei
950 province. For the other three months, temperatures are overestimated to varying degrees, both
951 during the day and at night (Fig. 2). The MYJ scheme performs best in all statistical parameters at
952 night (Fig. 19 b1-d1), while during the daytime, it slightly underperforms the YSU and ACM2
953 schemes in relative bias in January and April, but the difference is not very distinct. Therefore, for
954 the simulation of 2-m temperature in other three months, the MYJ scheme would be more
955 recommended. In the YRD region, the 2-m temperatures are overestimated during the daytime, the
956 BL schemes show overestimation at night, the MYJ scheme show underestimation, and the YSU
957 and ACM2 schemes perform optimally (Fig. 2 a2-d2). According to the Taylor statistical parameters,
958 it can be seen that the ACM2 scheme performs better than the YSU scheme in the four months, and
959 based on that, the ACM2 scheme is recommended (Fig. 19 a2-d2). The 2-m temperature in the SB
960 region during the daytime is the same as in the YRD region, and the ACM2 scheme performs
961 optimally (Fig. 19 a3-d3). However, the BL scheme performs optimally during the nighttime, except
962 in April (Fig. 19 b3). The PRD region differs from the other regions in that the temperature
963 simulation is significantly higher in January and April, and the MYJ scheme performs best in both
964 daytime and nighttime (Fig. 19 a4-b4). In contrast, the temperature simulation bias less in July and
965 October, and the BL scheme performs best (Fig. 19 c4-d4). The 2-m temperature are almost
966 underestimated during the daytime and overestimated for the nighttime in the NS region, and the
967 MYJ scheme outperforms other schemes on account of its large diurnal temperature range (Fig. 19
968 a5-d5). Of course, the BL scheme presents a slight advantage in the relative bias during the daytime
969 in January (Fig. 19 a5).

970 The results of 2-m relative humidity are relatively uniform, and the MYJ scheme shows optimal
971 simulation performance in almost all months in all regions. Except for July in the YRD region, July
972 and October in the PRD region, and January and April in the NS region (Fig. 19 c2, c4-d4, a5-b5).
973 For the simulation of 10-m wind speed and direction, the YSU scheme shows a very clear advantage,
974 which is outstanding in all regions and all months (Fig. 19).

975 Several sounding stations with large differences between the observed and simulated altitudes are
976 removed. Then, the stations in each region are averaged to induce the variation characteristics from
977 100 m to 2000 m in vertical.



978
979 **Figure 20. Statistics of temperature and wind speed in different layers at vertical height in January**
980 **(Winter), with circle size indicating the mean bias between simulations and observations, and**
981 **circles filled with color denoting the relative bias.**
982 The BL scheme has the smallest simulation bias for the temperature in the vertical direction in
983 January for the NCP region, and performs optimally, which is associated with the discussion of the
984 optimal scheme for the 2-m temperature (Fig. 20 a1) to some degree. While in all the other three
985 months, the MYJ scheme has the smallest bias and is consistent with the conclusion of the 2-m
986 temperature (Fig. S26-S28 a1). In the YRD region, there is no clear difference between the four
987 schemes for the simulation of temperature in the vertical direction, and the deviation of the
988 simulation in January is less than 0.1 K (Fig. 20 b1). The optimal scheme for 2-m temperature can
989 be considered as a representative choice. The MYJ scheme has a better simulation of the vertical
990 profile of the temperature that is somewhat different from the most preferred scheme of 2-m
991 temperature in the SB region (Fig. 20, S26-S28 c1). This is mainly because the selected sounding
992 stations are basically located in the basin area with low elevation, and the temperatures are
993 overestimated, as is the 2-m temperature (Fig. 5). If the stations around the basin are not considered,
994 the simulation of 2-m temperature will also be overestimated and the MYJ scheme also perform
995 optimally. There is no complex topography in the PRD region, the results from the sounding
996 stations and surface layer can be well echoed. In the vertical direction, the MYJ simulates the vertical profile



997 of temperature better, particularly in January and April (Fig. 20, S30, d1). While in July and October,
998 the simulation results of the four schemes have little difference, especially in the lower level, which
999 can be represented by the optimal scheme of 2-m temperature (Fig. S27-S28, d1). For the NS region,
1000 there is an overestimation in the lower levels and an underestimation in the upper levels for each
1001 month. The height of overestimation is lower in January and April, around 200 m, while it can reach
1002 around 500 m in July and October (Fig. 20, S26-S28, e1). The positive deviation decreases as the
1003 height increases, but after reaching a certain height, the negative deviation increases again. In the
1004 process of decreasing the positive deviation with height, the MYJ scheme performs the best, which
1005 is consistent with the 2-m temperature. While the BL scheme performs slightly better when the
1006 negative deviation gradually increases with height.

1007 For wind speed, the YSU scheme is optimal for 10-m wind speed for all regions and months.
1008 However, the quite different in terms of the variation of vertical wind speed. Throughout all regions
1009 and months, the simulation bias of the BL scheme is the smallest and closer to the observation,
1010 which is also the results obtained from the section 3.2.2 (Fig. 20, S26-S28 a2-e2). The stronger
1011 turbulent diffusion of the BL scheme at 08:00 makes the wind speed more uniformly mixed in the
1012 vertical direction. And the vertical variation characteristics at 08:00 can be extended to the whole
1013 night. But during the daytime, the result may not be the same, after all, the vertical mixing of the
1014 YSU scheme is stronger, and does not produce such a large wind speed gradient.

1015 In general, in the selection process of the PBL scheme, if the focus is on temperature variation, such
1016 as temperature inversion, the optimal scheme for both 2-m temperature and vertical temperature can
1017 be considered, and there is basically no significant difference. However, if the focus is on the
1018 variation of wind speed, wind energy, then the vertical wind speed and in the surface layer need to
1019 be evaluated and selected with comprehensive consideration.

1020 4 Conclusion

1021 The planetary boundary layer serves as a bridge between the ground and the free atmosphere, and
1022 its role cannot be ignored. Turbulence, as the primary motion within the PBL, controls the vertical
1023 mixing of heat, water vapor, momentum, and pollutants. Turbulence as a sub-grid-scale motion is
1024 usually parameterized in the model, i.e., PBL parameterization scheme. The most widely used
1025 mesoscale model (i.e., WRF), which has developed 12 schemes, includes nonlocal closure scheme,
1026 local closure scheme and hybrid nonlocal-local closure scheme. Across the world, there have been
1027 many evaluation studies for PBL parameterization schemes (reference Fig. 1 in Jia and Zhang, 2020).
1028 However, most of the studies have been conducted for individual stations in a small region with
1029 special individual cases for research and analysis, which are not well represented and applied.
1030 Meanwhile, there is a deficiency in understanding the mechanism of the scheme itself. In response,
1031 aiming at the current research deficiencies, four typical schemes (YSU, ACM2, BL and MYJ,



1032 covering each type scheme) are selected in this study to evaluate and analyze the near-surface
1033 meteorological parameters, vertical structure of the PBL, PBLH and turbulence diffusion in four
1034 months (i.e., January, April, July and October) in five typical regions of China (i.e., NCP, YRD, SB,
1035 PRD and NS regions).

1036 *a. 2-m temperature.* (1) In terms of time series and diurnal, the simulation results for July are better
1037 than the other three months, and better at night than daytime, with less deviation between simulation
1038 and observation. (2) in terms of regional distribution, temperatures at stations with higher elevations
1039 are easily underestimated (e.g., mountainous areas in the NCP region, areas around the SB basin,
1040 and the NS region), while overestimated at plains and basin (e.g., YRD, PRD and the SB basin
1041 regions), and the overestimation/underestimation is more significant during the daytime. (3) In
1042 terms of mechanism differences between schemes, the differences in the simulated temperatures of
1043 the four schemes are more pronounced at night. The differences in simulated temperatures between
1044 the nonlocal scheme mainly originate from downward shortwave radiation, while the effects of
1045 sensible heat flux (HFX) need to be further ruminated when comparing with the local closure
1046 scheme. when analyzing the HFX, the gradient of 2-m temperature and surface temperature, the
1047 variation of heat transfer coefficient need to be discussed in detail.

1048 *b. 2-m relative humidity.* The changes in relative humidity and temperature correspond to each other,
1049 and again the best simulation results are obtained in July. Except for the NS region, the relative
1050 humidity of the other regions is underestimated.

1051 *c. 10-m wind speed.* (1) The simulation bias is the largest for the MYJ scheme during the daytime
1052 (except for the NCP region), and the BL scheme presents the largest deviation at night in all regions,
1053 and the difference is not significant in the four months. The variation of 10-m wind speed is
1054 influenced by the momentum transfer coefficient, where a larger C_m produces stronger mixing and
1055 transports more momentum from the upper layers to the lower layers. For the YSU, ACM2 and BL
1056 schemes, the C_m and 10-m wind speed vary proportionally. In contrast, the MYJ scheme calculate
1057 principle of for MYJ scheme is different from the other schemes, and the C_m is larger than other
1058 months almost all day. However, the wind speed simulated by the MYJ scheme is maximum only
1059 during the daytime, which indicates that it is influenced by integrated similarity functions. (2) In
1060 terms of regional distribution, the wind speed is more overestimated in plains and basins, and less
1061 overestimated or even underestimated in mountainous areas. This is chiefly due to the influence of
1062 the model on terrain smoothing. (3) The overestimation of smaller wind speed at night is more
1063 obvious in the four schemes, primarily owing to the non-application of the MOST. At night, the
1064 turbulence intensity is disproportionate to the mean gradient, and the M-O similarity theory is no
1065 longer applicable.

1066 *d. 10-m wind direction.* The simulation of wind direction in January for the NCP region worse than
1067 the other three months, and the frequency of simulated northwest-north winds is overestimated by



1068 about 6.6%. For the YRD region, the frequency of northeasterly winds is overestimated. The
1069 simulation of wind direction in the SB region is not as good as other regions due to the complex
1070 topography. The frequency of northeasterly winds is overestimated in January and October in the
1071 PRD region, and that of southerly winds is overestimated in April and July. The wind direction is
1072 better simulated for the NS region, and the difference is not very obvious.

1073 *e. vertical distribution of PBL.* The model can reproduce the vertical structure of temperature well,
1074 but the inversion temperature at the lower levels of many stations in complex terrain cannot be
1075 simulated well, mainly because there is a certain difference in the terrain height between observation
1076 and simulation. At 08:00, the MYJ scheme simulates the lowest temperature and the BL scheme for
1077 the highest temperature, and the difference is more conspicuous at the lower levels. The vertical
1078 structure of the wind speed is clearly not as good as the temperature. The wind speed is almost
1079 always overestimated below 1000 m, except for the NS region. Unlike the 10-m wind speed, YSU
1080 has the smallest deviation from the 10-m wind speed, while the BL scheme has the smallest bias in
1081 the vertical direction. The BL scheme has the largest turbulent diffusion and the strongest mixing at
1082 08:00.

1083 *f. PBLH.* The PBLH calculated based on the observed data using the two methods are better in
1084 January than in the other three months, and in the NCP region than in the other four regions. The
1085 wind speed gradient simulated by the YSU scheme is large, resulting in a small Richardson number
1086 (Ri), making the height higher when Ri reaches 0.25, and the PBLH is higher than that of the ACM2
1087 scheme. The PBLH simulated by the BL scheme is closer to the observation because the temperature
1088 gradient is best simulated. The MYJ scheme results in a jagged variation of the PBLH due to the
1089 determination of the threshold and the vertical resolution, and this phenomenon is especially
1090 obvious at night. In terms of regional distribution, the PBLH is best simulated in the YRD region,
1091 followed by the PRD region and worst in the NS region. The results are similar in January and
1092 October, when the PBLH is lower and the simulations are better than those in April and July.

1093 *g. turbulent diffusion coefficient.* (1) The TDC simulated by the YSU and MYJ schemes is the
1094 largest during the daytime, followed by the BL scheme, and the smallest by the ACM2 scheme. The
1095 TDC simulated by the BL scheme is the largest at night, and the other three schemes are about the
1096 same. (2) The TDC is maximum in April and July, and minimum in January and October. (3) The
1097 obvious difference in PBLH affects the turbulent diffusion of the YSU and ACM2 schemes. It is
1098 worth noting that the YSU scheme calculates the TDC of momentum first, and then uses Prandtl
1099 number (Pr) to calculate the TDC of heat, while the ACM2 scheme calculates the TDC of both
1100 momentum and heat. (4) The difference between the BL and MYJ schemes is mainly reflected in
1101 the calculation principle of mixing length. The buoyancy effect mainly affects the mixing length
1102 scale in the BL scheme, and the mixing length scale of MYJ scheme is influenced by the TKE.
1103 For the discussion of the optimal scheme, different schemes need to be proposed for different



1104 parameters. (1) Temperature. The BL scheme is recommended for January in the NCP region,
1105 especially for the Beijing, and the MYJ scheme is recommended for the other three months. The
1106 simulation difference between the four schemes is small in the YRD region, and the ACM2 scheme
1107 is recommended. The topography is more complex in the SB region, but the MYJ scheme is
1108 recommended for most areas within the basin, and the BL scheme is recommended for the SB region
1109 if more around basin is involved. The MYJ scheme is recommended for the PRD region in January
1110 and April, and the BL scheme is recommended for July and October. In the NS region, the MYJ
1111 scheme is recommended. (2) Relative humidity. The MYJ scheme is recommended for all regions
1112 in four months. (3) Wind speed. The YSU scheme is recommended if the main concern is the surface
1113 layer, and the BL scheme is recommended if the focus on the variation of wind speed in the vertical
1114 direction.

1115

1116 Code and data availability

1117 The source code of WRF version 3.9.1 can be found on the following website:
1118 <https://www2.mmm.ucar.edu/wrf/users/download/>, and the model settings file is named
1119 “3.9.1_namelist.input”, which can be found in the Supplement. In addition, the hourly
1120 meteorological observation data and L-band radiosonde observation data provided by the Chinese
1121 Academy of Meteorological Sciences, are available at <https://doi.org/10.5281/zenodo.7792241> (Jia
1122 et al., 2023).

1123 Author contributions

1124 Development of the ideas and concepts behind this work was performed by all the authors. Model
1125 execution, data analysis and paper preparation were performed by WJ. XZ and HW provide
1126 computing resources, and offer advice and feedback. YW, DW, and JZ support the data. WZ, LZ,
1127 LG, YL, JW, YY, and YL provides suggestions. All authors contributed to the manuscript.

1128 Competing interests

1129 The authors declare that they have no conflict of interest.

1130 Acknowledgements.

1131 The work was carried out at the National Supercomputer Center in Tianjin, and the calculations
1132 were performed on TianHe-1 (A).



1133 Financial support

1134 This research is supported by NSFC Major Project (42090031), NSFC Project (U19A2044).

1135

1136 Reference

- 1137** Acevedo, O. C., Mahrt, L., Puhales, F. S., Costa, F. D., Medeiros, L. E., and Degrazia, G. A.
1138 Contrasting structures between the decoupled and coupled states of the stable boundary layer.
1139 *Quarterly Journal of the Royal Meteorological Society*, 142(695), 693-702. doi:10.1002/qj.2693,
1140 2015.
1141 Atkinson, B. W., and Zhang, W. J. Mesoscale shallow convection in the atmosphere. *Reviews of*
1142 *Geophysics*, 34(4), 403-431. doi:10.1029/96rg02623, 1996.
1143 Avolio, E., Federico, S., Miglietta, M. M., Lo Feudo, T., Calidonna, C. R., and Sempreviva, A. M.
1144 Sensitivity analysis of WRF model PBL schemes in simulating boundary-layer variables in southern
1145 Italy: An experimental campaign. *Atmospheric Research*, 192, 58-71.
1146 doi:10.1016/j.atmosres.2017.04.003, 2017.
1147 Bauer, P., Thorpe, A., and Brunet, G. The quiet revolution of numerical weather prediction. *Nature*,
1148 525(7567), 47-55. doi:10.1038/nature14956, 2015.
1149 Blackadar, A. K. The vertical distribution of wind and turbulent exchange in a neutral atmosphere.
1150 *Journal of Geophysical Research (1896-1977)*, 67(8), 3095-3102. doi:10.1029/JZ067i008p03095,
1151 1962.
1152 Bougeault, P., and Lacarrere, P. Parameterization of Orography-Induced Turbulence in a Mesobeta-
1153-Scale Model. *Monthly Weather Review*, 117(8), 1872-1890. doi:10.1175/1520-
1154 0493(1989)117<1872:Pooiti>2.0.Co;2, 1989.
1155 Broxton, P. D., Zeng, X., Sulla-Menashe, D., and Troch, P. A. A Global Land Cover Climatology
1156 Using MODIS Data. *Journal of Applied Meteorology and Climatology*, 53(6), 1593-1605.
1157 doi:10.1175/jamc-d-13-0270.1, 2014.
1158 Chen, F., and Dudhia, J. Coupling an Advanced Land Surface-Hydrology Model with the Penn
1159 State-NCAR MM5 Modeling System. Part I: Model Implementation and Sensitivity. *Monthly*
1160 *Weather Review*, 129(4), 569-585. doi:10.1175/1520-0493(2001)129<0569:Caalsh>2.0.Co;2, 2001.
1161 Cohen, A. E., Cavallo, S. M., Coniglio, M. C., and Brooks, H. E. A Review of Planetary Boundary
1162 Layer Parameterization Schemes and Their Sensitivity in Simulating Southeastern U.S. Cold Season
1163 Severe Weather Environments. *Weather and Forecasting*, 30(3), 591-612. doi:10.1175/waf-d-14-
1164 00105.1, 2015.
1165 Deardorff, J. W. Stratocumulus-capped mixed layers derived from a three-dimensional model.
1166 *Boundary-Layer Meteorology*, 18(4), 495-527. doi:10.1007/BF00119502, 1980.



- 1167** Diaz, L. R., Santos, D. C., Käfer, P. S., Iglesias, M. L., da Rocha, N. S., da Costa, S. T. L., et al.
1168 Reanalysis profile downscaling with WRF model and sensitivity to PBL parameterization schemes
1169 over a subtropical station. *Journal of Atmospheric and Solar-Terrestrial Physics*, 222, 105724.
1170 doi:10.1016/j.jastp.2021.105724, 2021.
- 1171** Ding, H., Cao, L., Jiang, H., Jia, W., Chen, Y., and An, J. Influence on the temperature estimation of
1172 the planetary boundary layer scheme with different minimum eddy diffusivity in WRF v3.9.1.1.
1173 *Geoscientific Model Development*, 14(10), 6135-6153. doi:10.5194/gmd-14-6135-2021, 2021.
- 1174** Emery, C., Liu, Z., Russell, A. G., Odman, M. T., Yarwood, G., and Kumar, N. Recommendations
1175 on statistics and benchmarks to assess photochemical model performance. *J Air Waste Manag Assoc*,
1176 67(5), 582-598. doi:10.1080/10962247.2016.1265027, 2017.
- 1177** Falasca, S., Gandolfi, I., Argentini, S., Barnaba, F., Casasanta, G., Di Liberto, L., et al. Sensitivity
1178 of near-surface meteorology to PBL schemes in WRF simulations in a port-industrial area with
1179 complex terrain. *Atmospheric Research*, 264, 105824. doi:10.1016/j.atmosres.2021.105824, 2021.
- 1180** Ferrero, E., Alessandrini, S., and Vandenberghe, F. Assessment of Planetary-Boundary-Layer
1181 Schemes in the Weather Research and Forecasting Model Within and Above an Urban Canopy Layer.
1182 *Boundary-Layer Meteorology*, 168(2), 289-319. doi:10.1007/s10546-018-0349-3, 2018.
- 1183** Grell, G. A., and Dévényi, D. A generalized approach to parameterizing convection combining
1184 ensemble and data assimilation techniques. *Geophysical Research Letters*, 29(14), 38-31-38-34.
1185 doi:<https://doi.org/10.1029/2002GL015311>, 2002.
- 1186** Gu, H., Jin, J., Wu, Y., Ek, M. B., and Subin, Z. M. Calibration and validation of lake surface
1187 temperature simulations with the coupled WRF-lake model. *Climatic Change*, 129(3), 471-483.
1188 doi:10.1007/s10584-013-0978-y, 2015.
- 1189** He, J., Chen, D., Gu, Y., Jia, H., Zhong, K., and Kang, Y. Evaluation of planetary boundary layer
1190 schemes in WRF model for simulating sea-land breeze in Shanghai, China. *Atmospheric Research*,
1191 278, 106337. doi:10.1016/j.atmosres.2022.106337, 2022.
- 1192** Hong, S.-Y., Noh, Y., and Dudhia, J. A New Vertical Diffusion Package with an Explicit Treatment
1193 of Entrainment Processes. *Monthly Weather Review*, 134(9), 2318-2341. doi:10.1175/mwr3199.1,
1194 2006.
- 1195** Hong, S.-Y., and Pan, H.-L. Nonlocal Boundary Layer Vertical Diffusion in a Medium-Range
1196 Forecast Model. *Monthly Weather Review*, 124(10), 2322-2339. doi:10.1175/1520-
1197 0493(1996)124<2322:Nblvdi>2.0.Co;2, 1996.
- 1198** Hong, S.-Y., and Shin, H. H. Analysis of Resolved and Parameterized Vertical Transports in
1199 Convective Boundary Layers at Gray-Zone Resolutions. *Journal of the Atmospheric Sciences*,
1200 70(10), 3248-3261. doi:10.1175/jas-d-12-0290.1, 2013.
- 1201** Hu, X.-M., Nielsen-Gammon, J. W., and Zhang, F. Evaluation of Three Planetary Boundary Layer
1202 Schemes in the WRF Model. *Journal of Applied Meteorology and Climatology*, 49(9), 1831-1844.



- 1203** doi:10.1175/2010jamc2432.1, 2010.
- 1204** Iacono, M. J., Delamere, J. S., Mlawer, E. J., Shephard, M. W., Clough, S. A., and Collins, W. D.
- 1205** Radiative forcing by long-lived greenhouse gases: Calculations with the AER radiative transfer
- 1206** models. *Journal of Geophysical Research: Atmospheres*, 113(D13).
- 1207** doi:<https://doi.org/10.1029/2008JD009944>, 2008.
- 1208** Janjić, Z. I. The Step-Mountain Coordinate: Physical Package. *Monthly Weather Review*, 118(7),
- 1209** 1429-1443. doi:10.1175/1520-0493(1990)118<1429:Tsmcpp>2.0.Co;2, 1990.
- 1210** Janjić, Z. I. The Step-Mountain Eta Coordinate Model: Further Developments of the Convection,
- 1211** Viscous Sublayer, and Turbulence Closure Schemes. *Monthly Weather Review*, 122(5), 927-945.
- 1212** doi:10.1175/1520-0493(1994)122<0927:Tsmecm>2.0.Co;2, 1994.
- 1213** Jia, W., and Zhang, X. The role of the planetary boundary layer parameterization schemes on the
- 1214** meteorological and aerosol pollution simulations: A review. *Atmospheric Research*, 239.
- 1215** doi:10.1016/j.atmosres.2020.104890, 2020.
- 1216** Jia, W., and Zhang, X. Impact of modified turbulent diffusion of PM2.5 aerosol in WRF-Chem
- 1217** simulations in eastern China. *Atmos. Chem. Phys.*, 21(22), 16827-16841. doi:10.5194/acp-21-
- 1218** 16827-2021, 2021.
- 1219** Jia, W., Zhang, X., Wang, H., Wang, Y., Wang, D., et al. Comprehensive evaluation of typical
- 1220** planetary boundary layer (PBL) parameterization schemes in China. Part I: Understanding
- 1221** expressiveness of schemes for different regions from the mechanism perspective. Zendo [data set],
- 1222** <https://doi.org/10.5281/zenodo.7792241>, 2023.
- 1223** Jiménez, P. A., and Dudhia, J. Improving the Representation of Resolved and Unresolved
- 1224** Topographic Effects on Surface Wind in the WRF Model. *Journal of Applied Meteorology and*
- 1225** *Climatology*, 51(2), 300-316. doi:10.1175/jamc-d-11-084.1, 2012.
- 1226** Kusaka, H., Kondo, H., Kikegawa, Y., and Kimura, F. A Simple Single-Layer Urban Canopy Model
- 1227** For Atmospheric Models: Comparison With Multi-Layer And Slab Models. *Boundary-Layer*
- 1228** *Meteorology*, 101(3), 329-358. doi:10.1023/A:1019207923078, 2001.
- 1229** Ma, Z., Zhao, C., Gong, J., Zhang, J., Li, Z., Sun, J., et al. Spin-up characteristics with three types
- 1230** of initial fields and the restart effects on forecast accuracy in the GRAPES global forecast system.
- 1231** *Geoscientific Model Development*, 14(1), 205-221. doi:10.5194/gmd-14-205-2021, 2021.
- 1232** Mass, C. F., Ovens, D., Westrick, K., and Colle, B. A. DOES INCREASING HORIZONTAL
- 1233** RESOLUTION PRODUCE MORE SKILLFUL FORECASTS?: The Results of Two Years of Real-
- 1234** Time Numerical Weather Prediction over the Pacific Northwest. *Bulletin of the American*
- 1235** *Meteorological Society*, 83(3), 407-430. doi:10.1175/1520-0477(2002)083<0407:Dihrpm>2.3.Co;2,
- 1236** 2002.
- 1237** Mellor, G. L., and Yamada, T. A Hierarchy of Turbulence Closure Models for Planetary Boundary
- 1238** Layers. *Journal of Atmospheric Sciences*, 31(7), 1791-1806. doi:10.1175/1520-



- 1239** 0469(1974)031<1791:Ahotcm>2.0.Co;2, 1974.
- 1240** Mellor, G. L., and Yamada, T. Development of a turbulence closure model for geophysical fluid
- 1241** problems. *Reviews of Geophysics*, 20(4), 851-875. doi:10.1029/RG020i004p00851, 1982.
- 1242** Meng Lu, Zhao Tianliang, Yang Xinghua, Liu Chong, He Qing, and Jingxin, D. An assessment of
- 1243** atmospheric boundary layer schemes over the Taklimakan Desert hinterland. *Journal of the*
- 1244** *Meteorological Sciences*, 38(2), 157-166. 2018.
- 1245** Monahan, A. H., and Abraham, C. Climatological Features of the Weakly and Very Stably Stratified
- 1246** Nocturnal Boundary Layers. Part II: Regime Occupation and Transition Statistics and the Influence
- 1247** of External Drivers. *Journal of the Atmospheric Sciences*, 76(11), 3485-3504. doi:10.1175/jas-d-19-
- 1248** 0078.1, 2019.
- 1249** Monin, A. S., and Obukhov, A. M. Basic laws of turbulent mixing in the surface layer of the
- 1250** atmosphere. *Akad. Nauk SSSR Trud. Geofiz. Inst*, 24, 163-187. 1954.
- 1251** Morrison, H., Thompson, G., and Tatarskii, V. Impact of Cloud Microphysics on the Development
- 1252** of Trailing Stratiform Precipitation in a Simulated Squall Line: Comparison of One- and Two-
- 1253** Moment Schemes. *Monthly Weather Review*, 137(3), 991-1007. doi:10.1175/2008mwr2556.1, 2009.
- 1254** Nakanishi, M., and Niino, H. An Improved Mellor–Yamada Level-3 Model with Condensation
- 1255** Physics: Its Design and Verification. *Boundary-Layer Meteorology*, 112(1), 1-31.
- 1256** doi:10.1023/B:BOUN.0000020164.04146.98, 2004.
- 1257** Nielsen-Gammon, J. W., Hu, X.-M., Zhang, F., and Pleim, J. E. Evaluation of Planetary Boundary
- 1258** Layer Scheme Sensitivities for the Purpose of Parameter Estimation. *Monthly Weather Review*,
- 1259** 138(9), 3400-3417. doi:10.1175/2010mwr3292.1, 2010.
- 1260** Noh, Y., Cheon, W. G., Hong, S. Y., and Raasch, S. Improvement of the K-profile Model for the
- 1261** Planetary Boundary Layer based on Large Eddy Simulation Data. *Boundary-Layer Meteorology*,
- 1262** 107(2), 401-427. doi:10.1023/A:1022146015946, 2003.
- 1263** Oke, T. R., Mills, G., Christen, A., and Voogt, J. A. (2017). *Urban Climates*. United States of
- 1264** America: Cambridge University
- 1265** Paulson, C. A. The Mathematical Representation of Wind Speed and Temperature Profiles in the
- 1266** Unstable Atmospheric Surface Layer. *Journal of Applied Meteorology and Climatology*, 9(6), 857-
- 1267** 861. doi:10.1175/1520-0450(1970)009<0857:Tmrows>2.0.Co;2, 1970.
- 1268** Persson, P. O. G., Walter, B., Bao, J. W., and Michelson, S. A. (2001). 3 *VALIDATION OF*
- 1269** *BOUNDARY-LAYER PARAMETERIZATIONS IN A MARITIME STORM USING AIRCRAFT DATA*.
- 1270** Pleim, J. E. A Combined Local and Nonlocal Closure Model for the Atmospheric Boundary Layer.
- 1271** Part I: Model Description and Testing. *Journal of Applied Meteorology and Climatology*, 46(9),
- 1272** 1383-1395. doi:10.1175/jam2539.1, 2007.
- 1273** Shen, W., Lu, Z., Ye, G., Zhang, Y., Chen, S., and Xu, J. (2022). Exploring the Impact of Planetary
- 1274** Boundary Layer Schemes on Rainfall Forecasts for Typhoon Mujigae, 2015. *Atmosphere*, 13(2).



- 1275** doi:10.3390/atmos13020220
- 1276** Stull, R. B. Transient Turbulence Theory. Part I: The Concept of Eddy-Mixing across Finite
- 1277** Distances. *Journal of Atmospheric Sciences*, 41(23), 3351-3367. doi:10.1175/1520-
- 1278** 0469(1984)041<3351:Ttpit>2.0.Co;2, 1984.
- 1279** Stull, R. B. (1988). *Turbulence Closure Techniques. An introduction to boundary layer meteorology*
- 1280** (Vol. 6). London: Atmospheric Sciences Library.
- 1281** Sun, J., Mahrt, L., Banta, R. M., and Pichugina, Y. L. Turbulence Regimes and Turbulence
- 1282** Intermittency in the Stable Boundary Layer during CASES-99. *Journal of the Atmospheric Sciences*,
- 1283** 69(1), 338-351. doi:10.1175/jas-d-11-082.1, 2012.
- 1284** Troen, I. B., and Mahrt, L. A simple model of the atmospheric boundary layer; sensitivity to surface
- 1285** evaporation. *Boundary-Layer Meteorology*, 37(1), 129-148. doi:10.1007/BF00122760, 1986.
- 1286** Vignon, E., van de Wiel, B. J. H., van Hooijdonk, I. G. S., Genthon, C., van der Linden, S. J. A.,
- 1287** van Hooft, J. A., et al. Stable boundary - layer regimes at Dome C, Antarctica: observation and
- 1288** analysis. *Quarterly Journal of the Royal Meteorological Society*, 143(704), 1241-1253.
- 1289** doi:10.1002/qj.2998, 2017.
- 1290** Wang, C., Shen, Y., Luo, F., Cao, L., Yan, J., and Jiang, H. Comparison and analysis of several
- 1291** planetary boundary layer schemes in WRF model between clear and overcast days. *Chinese J.*
- 1292** *Geophys. (in Chinese)*, 60(3), 924-934. 2017.
- 1293** Williams, P. D. Modelling climate change: the role of unresolved processes. *Philos Trans A Math*
- 1294** *Phys Eng Sci*, 363(1837), 2931-2946. doi:10.1098/rsta.2005.1676, 2005.
- 1295** Wyngaard, J. C., and Brost, R. A. Top-Down and Bottom-Up Diffusion of a Scalar in the Convective
- 1296** Boundary Layer. *Journal of Atmospheric Sciences*, 41(1), 102-112. doi:10.1175/1520-
- 1297** 0469(1984)041<0102:Tdabud>2.0.Co;2, 1984.
- 1298** Xie, B., Fung, J. C. H., Chan, A., and Lau, A. Evaluation of nonlocal and local planetary boundary
- 1299** layer schemes in the WRF model. *Journal of Geophysical Research: Atmospheres*, 117(D12).
- 1300** doi:10.1029/2011JD017080, 2012.
- 1301** Zhang, D., and Anthes, R. A. A High-Resolution Model of the Planetary Boundary Layer—
- 1302** Sensitivity Tests and Comparisons with SESAME-79 Data. *Journal of Applied Meteorology and*
- 1303** *Climatology*, 21(11), 1594-1609. doi:10.1175/1520-0450(1982)021<1594:Ahrmot>2.0.Co;2, 1982.
- 1304** Zhou, B., Zhu, K., and Xue, M. A Physically Based Horizontal Subgrid-Scale Turbulent Mixing
- 1305** Parameterization for the Convective Boundary Layer. *Journal of the Atmospheric Sciences*, 74(8),
- 1306** 2657-2674. doi:10.1175/jas-d-16-0324.1, 2017.
- 1307**